POLITECNICO DI TORINO

Master of Science in Energy and Nuclear Engineering

Master of Science Thesis

3D printed ceramic fuel and electrolysis cells for energy applications

Supervisor:

Prof. Federico Smeacetto

Dr. Marc Nuñez Eroles

Dr. Simone Anelli

Co – supervisor:

Prof. Albert Tarancòn Rubio

Prof. Monica Ferraris

Candidate:

Andrea Tegano

2020/2021

"*An energy system with high proportion of Renewable Energies inevitably requires plants that can supply electricity and heat reliably, quickly and in an environment friendly manner when the sun is not shining and the wind is not blowing".*

Professor Klaus Görner, scientific director of GWI.

Acknowledgements

I would like to express my gratitude to Prof. Federico Smeacetto and Prof. Albert Tarancòn Rubio who made this intercultural experience possible. I have learnt a lot from a technical and non-technical point of view, improving my skills as an engineer and as a human being.

Thanks to my university, the Politecnico di Torino, whose attentive and experienced professors have passed on to me knowledge in various sectors, from energy production and management to safety and economic aspects.

I am thankful to Dr. Marc Torrel who gave me the opportunity to participate in the whole process of prototyping 3D printed parts. I would also like to thank my supervisors Dr. Marc Nuñez Eroles and Dr. Simone Anelli for the training on inks preparation and on the whole set of machines, devoting their time to help me develop my thesis work and to satisfy my curiosity. I express my appreciation to the IREC staff for their friendly sharing of knowledge and moments outside the company. Particularly, to Diego, Gianfranco and Arianna.

Thanks to my friends and my girlfriend Chiara who supported and endured me before and during my time at university, sharing fun and unforgettable moments.

I am grateful to my family. Thanks to you Mom and Dad who have made it possible to study and ensure a good lifestyle amidst sacrifices and joys. I hope one day to be able to reward you by reciprocating your efforts. Of course, thanks to my sister Stefania always there to support me in difficult moments, and thanks to my brother-in-law Simone whose presence brings happiness and tranquillity to our family.

I dedicate this thesis to my grandmother Sasa and my aunt Lina, women who with their love and attention taught me about traditions and manners.

Vorrei esprimere la mia gratitudine al Prof. Federico Smeacetto e al Prof. Albert Tarancòn Rubio che hanno reso possibile questa esperienza interculturale. Ho imparato molto dal punto di vista tecnico e non tecnico, migliorando le mie capacità come ingegnere e come essere umano.

Grazie alla mia università, il Politecnico di Torino, i cui professori attenti ed esperti mi hanno trasmesso conoscenze in vari settori, dalla produzione e gestione dell'energia alla sicurezza e agli aspetti economici.

Sono grato al dottor Marc Torrel che mi ha dato l'opportunità di partecipare all'intero processo di prototipazione di parti stampate in 3D. Vorrei anche ringraziare i miei supervisori Dr. Marc Nuñez Eroles e Dr. Simone Anelli per la formazione sulla preparazione degli inchiostri e sull'intero set di macchine, dedicando il loro tempo per aiutarmi a sviluppare il mio lavoro di tesi e per soddisfare la mia curiosità. Esprimo il mio apprezzamento al personale dell'IREC per la loro amichevole condivisione di conoscenze e momenti fuori dall'azienda. In particolare, a Diego, Gianfranco e Arianna.

Grazie ai miei amici e alla mia ragazza Chiara che mi hanno sostenuto e sopportato prima e durante il mio periodo universitario, condividendo momenti divertenti e indimenticabili.

Sono grato alla mia famiglia. Grazie a voi Mamma e Papà che avete reso possibile studiare e garantire un buon stile di vita tra sacrifici e gioie. Spero un giorno di potervi ricompensare ricambiando i vostri sforzi. Naturalmente grazie a mia sorella Stefania sempre presente a sostenermi nei momenti difficili, e grazie a mio cognato Simone la cui presenza porta felicità e tranquillità alla nostra famiglia.

Dedico questa tesi a mia nonna Sasa e a mia zia Lina, donne che con il loro amore e attenzione mi hanno insegnato le tradizioni e le buone maniere.

Abstract

Nowadays, the consolidated awareness of climate change caused by anthropogenic activities promotes the development of human society towards a climate-neutral scenario with zero greenhouse gas emissions. In this scope the integration of renewable energy (RE) sources in the power system has become a key strategy to reduce fossil fuel consumption and promote the transition towards a sustainable energy system.

However, RE are intrinsically limited by their own intermittent nature. For this reason, clean methods for energy conversion and storage are being developed. Particularly the utilization of hydrogen as energy vector has emerged as an effective and environmentally friendly solution. Among various technologies developed for hydrogen production, Solid Oxide Cells (SOCs) are interesting devices due to their reversibility and high efficiency granted by the high operating temperature. Nevertheless, the production of these multi-material energy devices continues to be a drawback, as it involves a costly and time-consuming process requiring several stages of production and assembly.

Currently, 3D printing is leading the prototyping solutions in many research and development laboratories. The 3D printing community has experienced an important surge in the last years, becoming easily accessible. 3D printing covers a wide range of materials among which the typical ceramic materials used for SOC application. In particular for ceramic materials, some of the most complex geometries are only manufacturable using 3D printing.

This work focuses on the implementation of Additive Manufacturing (AM) by 3D printing for the fabrication of SOCs.

Stereolithography (SL) has been used for producing innovative SOC designs. Specifically, a flat large area electrolyte (60x95 mm^2) of 3YSZ was fabricated and it was characterised in symmetrical configuration obtaining an electrolyte Area Specific Resistance (ASR) of $\cong$ 11 Ωcm^2 at 800°C. Moreover, spiral designed cells were built and functionalized.

The utilization of this innovative technology, which involves flexibility in design, fabrication of complex geometry with high resolution and maximum material savings, will open new degrees of freedom in the design of SOC cells, providing advantages both in processing and device performance.

Table of contents

Acronym list

3D	Three dimensional
3DP	Three-dimensional printing
AC	Alternated Current
AC	Alkaline Cell
AM	Additive Manufacturing
APU	Auxiliary Power Units
ASR	Area Specific Resistance
BSE	Backscattered Electrons
C	Capacitance
CAD	Computer Aided Design
CCS	Carbon Capture and Storage
CGO	Gadolinium Doped Ceria
CHP	Combined Heat and Power
CPE	Constant Phase Element
Crofer22	Chromium (22%)-Ferritic
CSL	Ceramic Stereolithography
CTE	Coefficient of Thermal Expansion
CVD	Chemical Vapor Deposition
DC	Direct Current
DMC	Direct Machine Control
DIW	Direct Ink writing
DMLS	Direct Metal Laser Sintering
DOD	Drop on Demand
EHT	Electron High Tension
EIS	Electrochemical Impedance Spectroscopy
FDM	Fused Deposition Modelling
GDC	Gadolinium Doped Ceria
GT	Gas turbine
IEA	International Energy Agency
L	Inductance
LHV	Low Heating value
LSCF	Lanthanum Strontium Cobalt Ferrite
LSM/YSZ	Lanthanum Strontium-Manganite-Yttrium Stabilized Zirconium composite
MCC	Molten Carbonate
MIEC	Mixed Ionic Electronic Conductor
MSc	Master of Science
Ni/YSZ	Nickel- Yttrium Stabilized Zirconium composite
P2G	Power – to – Gas
P2P	Power – to – Power
PEMC	Polymeric Electrolyte Membrane cell
PG	Propylene Glycol
PMMA	Polymethyl Methacrylate
PVP	Polyvinylpyrrolidone
R	Resistance
RC	Robocasting
RE	Renewable Energy
RES	Renewable Energy Sources
REDOX	REDuction – OXidation
rSOC	reversible Solid Oxide Cell
ScSZ	Scandia Stabilized Zirconia
SE	Secondary Electrons
SEM	Scanning Electron Microscopy
SL	Stereolithography
SLA	Stereolithography Apparatus
SLM	Selective Laser Melting
SLS	Selective Laser Sintering
SNG	Synthetic Natural Gas
SoA	State of the Art

SOCs	Solid Oxide Cells
SOECs	Solid Oxide Electrolytic Cells
SOFCs	Solid Oxide Fuel Cells
STL	Standard Triangulation Language
TPB	Triple Phase Boundary
TSR	Thermal Shock Resistance
UV	Ultraviolet
VRE	Variable Renewable Electricity
YSZ	Yttrium Stabilized Zirconium

Executive summary

The well-known effects and causes of climate change would lead to reductions in greenhouse gas emissions and energy consumption in end-user sectors, decarbonisation and reduction in net emissions in the energy supply chain. The implementation of low greenhouse gas emission energy supply technologies, such as renewable energy (RE) and nuclear energy, serves the purpose of climate change mitigation. However, RE production does not always meet the user's energy demand due to its discontinuous production and different strategies to storage the Variable Renewable Electricity (VRE) have been proposed.

Hydrogen production by electrolysis of water was proven to be an effective tool to store excess energy over a long period (e.g. months), offsetting the loss of flexibility resulting from less use of fossil fuels while decarbonising many sectors of the economy. Electrochemical cells are very efficient devices to produce hydrogen from water electrolysis. Their scalability and flexibility combined with their reversible nature, make them also suitable for using this energy carrier for energy production, reducing energy supply costs and power losses in transport. Over the years, various electrochemical cells have been developed but one of them stands out among all, due to its feedstock fuel flexibility, no leakage and flooding problems and higher efficiency: Solid Oxide Cells (SOCs).

SOCs are electrochemical cells which work at high temperature (500 - 1000°C) and are composed of at least four ceramic based materials with different requirements. The manufacturing of this devices requires several production stages which are costly and time-consuming. The implementation of Additive Manufacturing (AM) to develop these electrochemical devices allows to produce advanced and structurally optimised SOCs with high resolution and maximum material savings.

This work has been carried out at "*Institut de Recerca en Energia de Catalunya - IREC*" (Barcelona) for producing electrolytes with innovative design and pursuing high throughput automated production in a single step in the field of energy conversion. Ceramic large area and spiral cells have been fabricated by means of Stereolithography (SL) technique to investigate the complete standard stacks in a single production step and to fabricate a small-volume fuel cell with high inlet fuel percentage consumption and low volume to active surface ratio. UV curing layer by layer the 3YSZ paste through the "*Ceramaker*" printer, large area and spiral electrolytes were successfully printed with high resolution. Subsequently the parts have been post-processed, including cleaning, debinding and sintering up to 1450°C.

The large area electrolyte was subsequently assembled with a commercial LSM/YSZ cathode for Electrochemical Impedance Spectroscopy (EIS) in symmetrical configuration. By fitting EIS measurements carried out in air in the range of 650-950°C, the cell was characterised achieving at 800°C a comparable Area Specific Resistance (ASR) of the electrolyte about 11 Ωcm^2.

Following various attempts to infiltrate this pioneering design, the spiral electrolyte was anodic functionalised with 28% vol. of solid load NiO/YSZ ink (I3), optimized in terms of microstructural, rheological and thermal properties. The anodic ink was deposited by injection and sintered at 1250°C, obtaining an infiltrated self-supporting spiral electrolyte for the first time. This design, challenging to post-process, established the potential AM techniques to produce complex shapes, where further geometry optimisations could enable a power increase of around 600% compared to a simple tubular cell.

.

Chapter 1| Introduction

1.1. General introduction

Nowadays the present energy production system is dominated by the utilization of fossil fuels, which provide more than the 80% of the energy globally consumed [1]. The utilization of fossil fuels represents an environmental risk and in the recent years the awareness of this concern, connected to global warming, has become more and more predominant. Several world agreements have been developed to reduce the emission of greenhouse gasses (GHG) and the consumption of fossil fuels [2]. The energy supply sector[1] significantly contributes to the emission of polluting gas emissions [3]. In order to reduce GHG emissions coming from the energy sector, the research has been focused on efficiency improvements for production, implementation of carbon dioxide capture and storage (CCS) and low-GHG energy supply technologies such as renewable energy (RE) and nuclear power [4].

However, the intermittent nature of renewable energy sources (e.g., solar and wind energies), made necessary the research and the implementation of clean strategies for the storage of the peak production excess and the reutilization of such an energy when is required. Batteries, supercapacitors, gas batteries, and the utilization of hydrogen or other biofuels as energy vector are the main candidates for the clean storage of energy.

Hydrogen has demonstrated to be an efficient alternative to fossil fuels due to its high energy mass density. In fact, 1 kg of hydrogen can produce energy ≈100 MJ, while the same amount of petroleum can produce ≈46 MJ [5]. Hydrogen is a flexible energy carrier that can be produced from any dominant primary energy source and can help to decarbonise many sectors including transport, industry, agriculture, and energy generation [6]. Nowadays 95% of the hydrogen produced comes from reforming hydrocarbons [7], which represents an environmental risk due to the amount of CO2 released in the atmosphere. Figure 1 illustrates how hydrogen could interconnect the different energy levels of a production system: the heat network, the electricity grid and the utilization of biofuels.

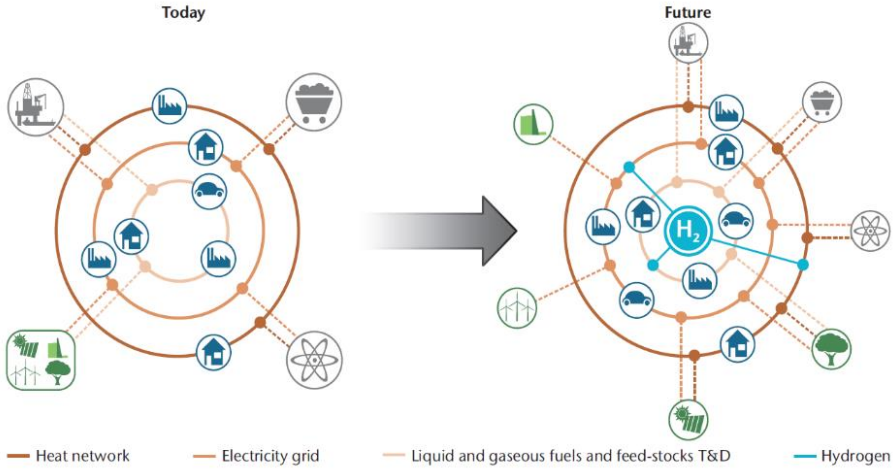

Figure 1|Energy system today and in the future. The utilization of hydrogen as energy vector allows to connect the heat network with the electricity grid and the utilization of liquid and gaseous bio-fuels- Source: IEA (2015) [8]

[1] All energy extraction, conversion, storage, transmission, and distribution processes that deliver final energy to the end-use sectors.

In order to avoid dependence on fossil fuels, and to use hydrogen as an enviromentally friendly energy vector, alternative production techniques have been developed. Examples include water electrolysis or chemical looping, photobiological water splitting and photoelectrochemical water splitting [9]. The production of hydrogen, without CO2 emission and by using RE sources, is called green hydrogen [10]. To this regard, the utilization of hydrogen can play a key role in several pathways [8] as:

- *Power – to – power (P2P):* Electricity is converted into hydrogen, then stored in a tank (liquid or gas) and re-converted as needed (i.e., electricity peak demand) using a fuel cell or a hydrogen gas turbine.
- *Power – to – gas (P2G):* Use of electricity for conversion into hydrogen to be injected directly into the existing natural gas network (Blending) or to produce Synthetic Natural Gas (SNG) using a system consisting of SOEC and thermo - catalytic reactors (Co - electrolysis + methanation process), requiring in addition only water and CO_2 [11].
- *Power-to-fuel:* electricity is transformed into hydrogen and then used for fuel cell electric vehicle. These vehicles allow for a refuelling time lower than 10 minutes and a range over 450 km with a full tank [12, 13].
- *Power-to-feedstock:* electricity is used to produce hydrogen and then used as a feedstock, for example in the chemical industry. Hydrogen is used to produce ammonia, methanol, fertilizers for agriculture or for the metals treatments in the metallurgy industry.

Figure 2 shows the role of electrolysis cells in the power to gas system. The clean hydrogen can be stored for a later use or converted in directly into energy with a fuel cell.

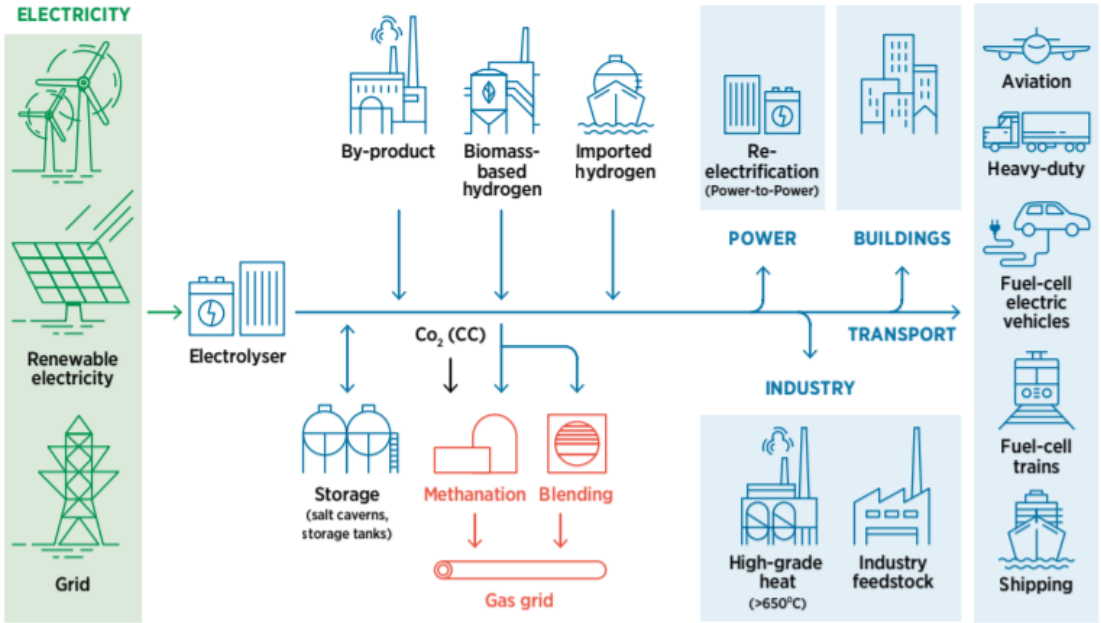

Figure 2|Integration of VRE into end-uses by means of hydrogen - Source: IRENA (2019) [14]. The figure shows the exploitation of VRE by an electrolyser, which produces what is called, green hydrogen (blue line). The hydrogen produced by the electrolyser in combination with other forms of hydrogen generation can be stored, converted, or supplied directly to end users.

1.2. Electrolysis and fuel cells

Electrolysis and fuel cells are reversible electrochemical devices capable of converting the chemical energy of a fuel directly into electrical energy (Galvanic or Fuel cell mode) or vice versa (electrolysis cell mode). The abundance and low cost of primary energy sources have limited the development of this technology [15]. However, in the last 20 years, the limitation represented by the intermittent nature of RES pointed out the necessity to develop clean strategies for storage and conversion. Electrolysis and fuel cells demonstrate to be the best alternative for a clean and sustainable hydrogen use and production.

An elementary electrochemical cell is composed of two electrodes, where oxidation (anode)-reduction (cathode) reactions take place. The electrodes are connected by an external circuit and separated by an ionic conductor called electrolyte. Considering a cell with this structure, when REDOX occurs spontaneously the chemical energy is converted into electrical energy, such devices can work also in the opposite direction. In this case electrical energy (current) is applied to the cell and converted into chemical energy (chemical products). As a result of the reversibility of this device, the terms anode and cathode are usually avoided. The more common terminology nowadays involves the terms "fuel electrode" and "oxygen electrode", taking into consideration the gases which flow at the two electrodes. One can notice the partial reactions happening at the oxygen (B1) and at the fuel electrode (B2) and the overall spontaneous reaction of formation of water (B3) in the case of fuel cell configuration.

$\frac{1}{2}O_2 + 2e^- \rightleftarrows O^{2-}$ (oxygen reduction) (B1)

$H_2 \rightleftarrows 2H^+ + 2e^-$ (hydrogen oxidation) (B2)

$H_2 + \frac{1}{2}O_2 \rightleftarrows H_2O$ (overall reaction) (B3)

As shown in figure 3, the cells are stacked and connected in series by an interconnector that allows gas distribution and electrical connection, forming the so called Single Repeated Unit (SRU). This is done to increase the voltage and thus the power or productivity of this device. To satisfy high power demand, the stacks are connected to each other to form modules, and the stack as well as the modules are managed with auxiliary components forming the production system.

Figure 3| Fuel cell scalability concept - Source: Bloom energy [16]

Fuel cells can cover a wide range of applications [17] such as stationary small to large scale Combined Heat and Power (CHP) production, Auxiliary Power Units (APU), vehicle traction and portable devices. By comparing traditional internal combustion engines with these scalable and flexible energy devices fuel cells can reach the double electrical performance with low environmental impact (silent with low emission of air pollutants). In addition, the efficiency is independent from the energy load, the plant size and installed power, in contrast to conventional

systems [18]. The power plants can be located nearby the end – users, reducing transport power losses and energy supply cost.

Moreover, the interest in their functioning as electrolysers is as great, if not greater, because using water electrolysis to convert the Variable Renewable Electricity (VRE) surplus into hydrogen and oxygen, it is possible store this energy for a long time (days, months) compensating the loss of flexibility resulting from the reduced use of fossil fuels [8].

Over the years, various types of gas batteries have been developed differentiated by the type of electrolyte employed and operative temperature (see table 1) [19]. As an example, the Polymeric Electrolyte Membrane cell (PEMC) has a polymeric electrolyte capable to conduct hydrogen ions (H^+) and it operates at temperature of about 60-80°C, whereas Alkaline cell (AC) has liquid electrolyte and works in the temperature range of 70-130 °C transferring OH^-ions. Molten Carbonate (MCC) uses a molten salt CO_3^{2-}ionic conductor under the intermediate temperature of 550-650°C. Solid Oxide cells (SOCs) operate at high temperature about 500-1000°C and employ a solid ceramic electrolyte to transfer oxygen ions (O^{2-}).

Gas Battery	***Operating temperature (°C)***	***Charge carrier***	***Power (kW)***	***Efficiency [LHV] (%)***	***Application***
Polymer Electrolyte Membrane cell	60-80	H^+	0.01-250	40-55	Portable, mobile, low power generation
Alkaline cell	70-130	OH^-	0.1-50	50-70	Mobile, space, military
Molten Carbonate cell	550-650	CO_3^{2-}	200-100,000	50-60	Large scale power generation
Solid Oxide cell	500-1000	O^{2-}	0.5-2000	40-70	Vehicle auxiliary power units, medium to large power generation and CHP, off-grid power and micro-CHP

Table 1| Comparison of different types of gas battery [19]. In the table are shown the main existing types of fuel and electrolysis cell, which are Polymeric electrolyte membrane, Alkaline, Molten Carbonate and Solid Oxide.

Currently, these types of gas batteries have been used for local or distributed energy production, due to their high efficiency. However, one of them stands out among all, due to its feedstock fuel flexibility, no leakage and flooding problems and higher efficiency: Solid Oxide Cells (SOCs).

Unlike low temperature fuel cells, due to solid oxide electrolyte used, this device operates at high temperature which kinetically promotes reforming reactions. The reaction of reforming enables the use of low molecular weight hydrocarbons as fuel, including natural gas, biogas, ethanol etc., which can be obtained from biochemical or thermochemical processes by converting biomass, coal or municipal waste [20, 21]. A ready-to-use SOFCs system can achieve an electrical efficiency (LHV) of 40 to 60%. Furthermore, considering CHP operation,

the efficiency can reach values above 90%(LHV), making SOFC one of the most efficient power generation device currently available. By integrating SOFCs into existing power plants through the combustor replacement (hybrid SOFC – GT system), the thermal efficiency of conventional power plants can be doubled [22] and Carbon Capture & Storage (CCS) can be easily achieved.

In addition, in the electrolyser mode, the high temperature range of operation can grant conversion efficiencies higher than 80% (LHV) [23]. SOEC can also be used for co-electrolysis of steam and carbon dioxide to produce hydrogen and carbon monoxide. The H2+CO mixture is called synthetic gas and it is the base for the production of a wide number of chemicals [24].

1.3. Structure of a Solid Oxide Cell

SOCs are electrochemical devices composed of two porous electrodes oxygen and fuel electrodes) which are separated by a solid oxide electrolyte capable to conduct oxygen ions (O^{2-}). In galvanic cell mode, SOCs are named Solid Oxide Fuel Cells (SOFCs). In a SOFC air is provided at the oxygen electrode, where the Oxygen Reduction Reaction (ORR) takes place. The O^{2-} ions move through the electrolyte to the fuel electrode, where hydrogen is fed. The spontaneous reaction of formation of water releases electrons to the external circuit and steam as sub-product. Conversely, a SOC which is working in electrolysis mode is called Solid Oxide Electrolysis Cell (SOEC). Here, power is supplied to the cell to split water into hydrogen, produced in the fuel electrode, and oxygen at the oxygen electrode. As a result of the reversibility of this device, SOC is often referred to as rSOC [25].

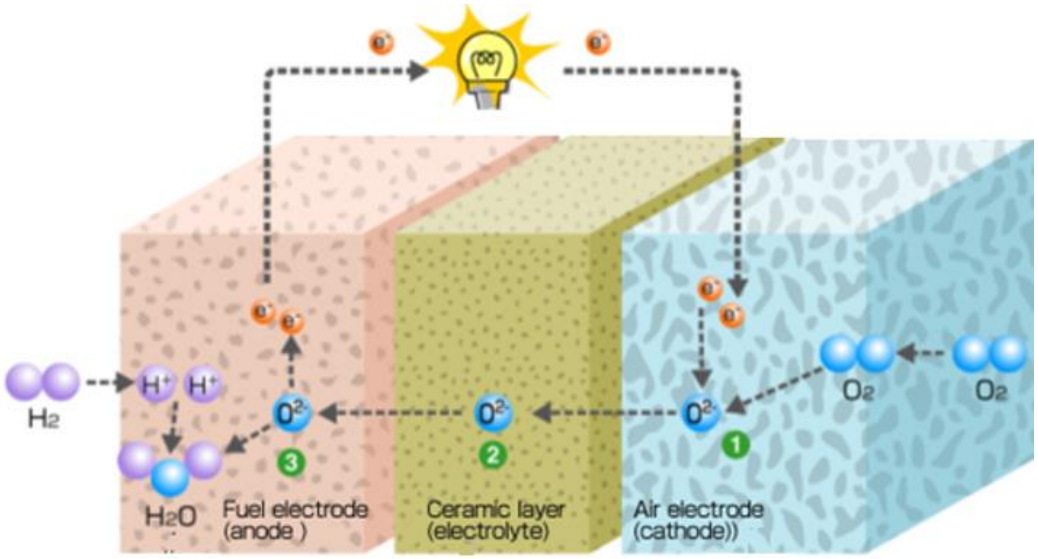

Figure 4| Schematic showing working principle of SOC operating in galvanic mode. One can observe the fuel electrode where hydrogen is consumed to release electrons and produce water. At the oxygen electrode molecular oxygen is reduced into O2- anions which travel through the dense ceramic electrolyte. - Source OSAKA GAS- [26]

Despite the thermodynamic advantages provided by the high operating temperatures, SOCs presents different technical challenges to find suitable materials and avoid degradation problems. The main issues of SOC devices are the high cost of the materials and the reliability for long-term operation [27, 28].

A single SOC cell usually requires the assembly at least of four different components, which should present suitable mechanical, chemical, physical, electrical and electrochemical properties in the operating temperature range [13]. The electrolyte should exhibit good ionic

conductivity and a good density to prevent gas mixing. On the other hand, the electrodes should present a porous structure to ensure the permeability of the gases [29]. In addition, the SOCs stack consisting of selected single cells must be designed to achieve the desired electrical and electrochemical performance. Furthermore, chemical stability, thermal management, gas flow distribution and pressure drop should be considered, as well as mechanical/structural integrity to satisfy specific production requirements.

The most common material [25] currently used that partially match the cell requirements for electrolyte is Yttrium Stabilized Zirconium oxide (YSZ, often 8 mol% Y2O3). YSZ present good ionic conductivity and exhibits the desired phase stability in both oxidizing and reducing atmosphere [30]. Another typical material used as electrolyte is Scandia Stabilized Zirconia (ScSZ, usually 9 mol% Sc2O3) that present a higher ionic conductivity but is much more expensive.

The interface region between the electrodes and the electrolyte, where the gases can penetrate and both ionic and electronic conductivity are provided, forms so-called triple phase boundary (TPB) [31]. The TPB is the active region of the electrode and its extension is one of the strategies to improve the performance of a SOC device. To increase the TPB area the two electrodes are usually composites formed by different materials. The electrodes should usually provide mechanical stability, a porous structure, and both ionic/electronic conductivity. The state-of-the-art materials for the fuel electrode are NiO and -YSZ. YSZ provides the ionic conductivity and the mechanical compatibility with the electrolyte. NiO becomes metallic Ni upon reduction and it provides the electrical conductivity and the catalytic activity.

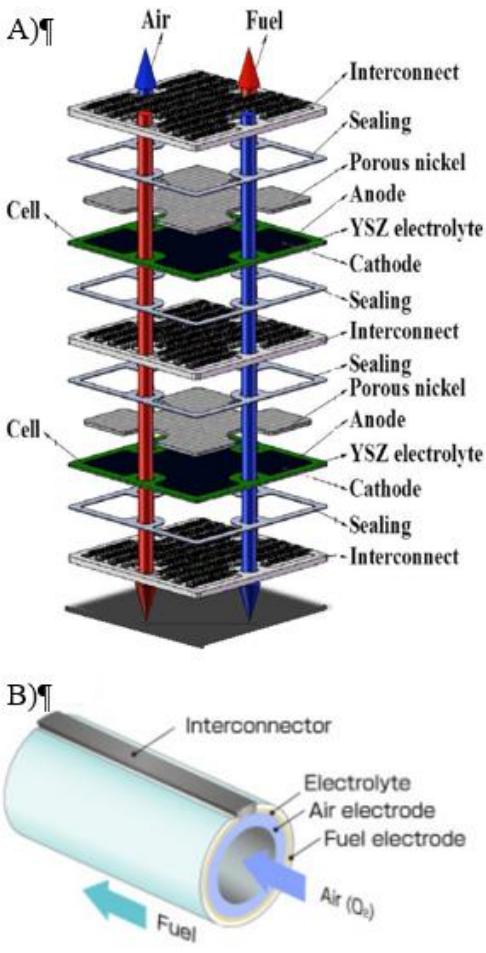

Figure 5| Types of cell design: A) Planar [35], B) Tubular [26]

The oxygen electrode is formed by perovskite materials such Lanthanum Strontium-Manganite (LSM) and Lanthanum-Strontium-Cobalt-Ferrite (LSCF). LSCF at high temperature is a Mixed Ionic/Electronic Conductor (MIEC). The utilization of MIEC materials can expand the TPB, offering better performance compared with mostly electronic conductors [32]. Furthermore, MIECs are often combined with pure ionic conductors (e.g., YSZ, CGO) in order to further enhance the TPB area and to increase the compatibility with respect to the other parts of the cell. Due to high electrical conductivity and similar thermal expansion behaviour with other cell components [33], materials such as Crofer22APU are used as interconnector.

The main cost related to the production of a SOC device is closely related to the high energy and long manufacture processes of the stacks and their power size. Conventionally, the manufacture of SOC stacks is a costly and time-consuming multi-stage production process. The fabrication includes casting, screen printing, moulding, various heat treatments and manual stack assembly. This results in more than 100 steps that are involved for the fabrication, resulting in difficult quality control and product standardisation [34]. Materials selection, cell configuration and cell design closely impact the fabrication process selection, process sequences and

the cell performance, requiring sometimes further components such as sealing in the planar configuration [35]. To this regard, the State of Art of SOC involves the use of tubular (figure 5-A) and planar (figure 5-B) design and configuration as self-supporting (figure 6-A) or external-supporting (figure 6-B).

Moreover, it is essential to try to produce and maintain the desired microstructure (i.e., open pore structure of the electrodes), cell shape tolerances, thickness uniformity, adhesion, while ensuring a reproducible process with a high production rate.

Currently, the manufacturing of ceramic components and composites is based on two types of approach: i) particulate approach, involving powders compaction and densification at high temperature; ii) deposition approach, consisting in the formation of layers on a substrate by chemical or physical phenomena. The most common manufacturing techniques based on particulate approach are tape casting, tape calendaring and screen printing, for the planar configuration, while cells with tubular configuration are usually fabricated by extrusions.

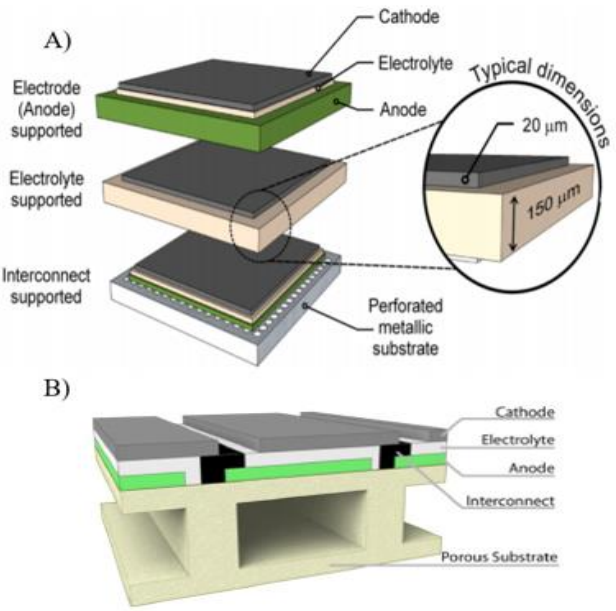

Figure 6| Cell configuration in which figure A) shows the self-supporting configuration and figure B) the segmented cell in series with external supporting-configuration. Note that the cathode support is missing, as this configuration was abandoned in the early 2000s due to its transport problems and its chemical reactivity with the YSZ electrolyte – Sources [19] [32]

Tape casting is an easily replicable and cost-effective method mainly implemented to manufacturing of the support layer (primary layer) and/or functional layer (additional layer). The process consists (see figure 7a) in casting onto a moving tape a slurry containing the ceramic powder(s), the solvent and other additives: pore formers, to create porous structures, dispersant to avoid agglomeration, binder, plasticizer to change the rheological properties of the slurry [36]. By controlling the thickness through a doctor blade from few to several hundred of microns, the slurry is spread on the tape and subsequently dried in an oven, leaving the solvent to evaporate. The dried tape also referred to as green tape, is sintered to achieve the desired density. In this technique the solvent used can be organic or aqueous based [37].

Analogous to tape casting, tape calendaring (see figure 7b) produces thin foils. Controlling the thermoplastic based tape thickness by the spacing between rollers, this technique also allows the co-rolling of more than one layer.

Screen printing (see figure 7c) is a stencil process where the ink composed by powders, binders and solvents, is forced applying a pressure through a screen by squeegee. The Squeegee controls the spreads of the ink across the screen and removes the excess ink while the applied pressure controls the thickness [38]. It is often coupled with tape casting (see figure 8) to deposit a thinner layer (i.e., diffusion barriers, cathode) on the top of the substrate (i.e., anode, electrolyte).

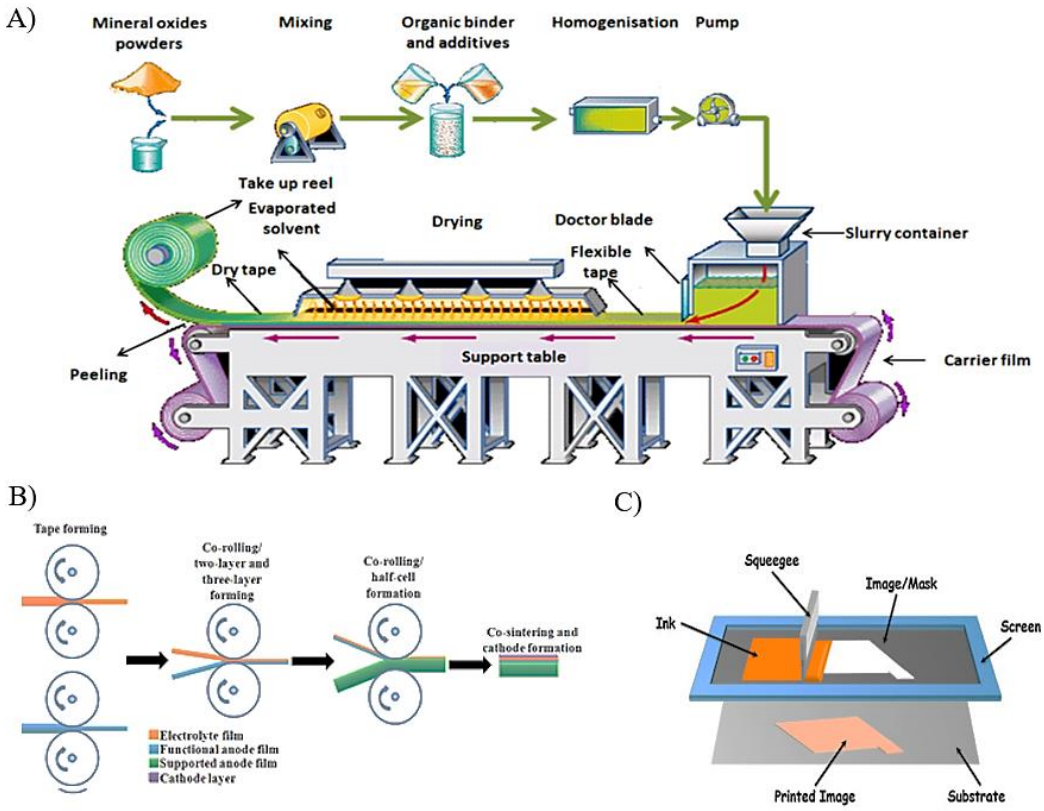

Figure 7| Particulate approach methods: A) Tape casting [39]; B) Tape calendaring [40]; C) Screen printing [41]

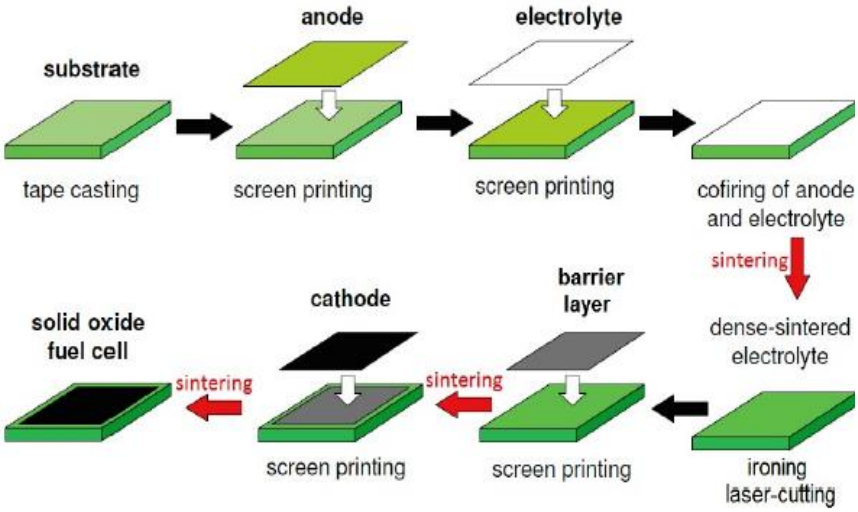

Figure 8|Schematic cell manufacturing process which uses tape casting and screen-printing techniques [42]

To regard the state-of-the-art SOCs (SoA SOCs) system cost expenditure (CAPEX), the total cost is about 7000-8000 €/kW, of which stack is the single most expensive component [43]. This cost can be reduced by introducing high throughput automated production and quality control.

In the recent years, the utilization of Additive Manufacturing (AM) techniques allow to develop next generation SOCs, structurally optimising and developing advanced architectures reducing the total cost and environmental footprint [44, 45].

1.4. 3D printing techniques overview

Additive manufacturing (AM) is a technique for fabricating three – dimensional solid objects by adding successive layer of material starting from a Computer Aided Design (CAD) model. This method represents a family of flexible manufacturing techniques and it has been proposed and developed by Charles Hull in 1986 in a process known as stereolithography (SL) [46, 47].

Initially, 3D printing has been widely used by architects and designers to produce quickly and cost – effective aesthetic and functional prototypes. In the few past years, this technique has been fully used in the jewellery, footwear, industrial design, architecture, engineering, automotive, aerospace, dental and medical sectors, replacing traditional fabrication processes that are mostly based on subtractive processes such as cutting or drilling methods [48]. The growing acceptance of 3D machining over traditional techniques is attributed to several benefits including flexibility in design, personal customisation, fabrication of complex geometry with high resolution and maximum material savings. In addition, the Internet increases the possibilities to share the design and modification of the objects additively produced [49], by allowing their use in any place and at any time in the product life cycle, from pre-production to full scale production and customization in post-production. The implementation of 3DP for these highly demand applications can significantly reduce the loss of precious advanced materials (production costs), simplifying the design for manufacturing, while reducing the number of fabrication steps (shaping, thermal treatments and assembly) [50].

Although there is a clear interest in additive manufacturing techniques for energy device applications, over the last three decades AM has been developed and marketed mainly for polymeric and metal structural parts. As a result, functional materials and systems suitable for 3D printing of energy devices remained an almost unexplored field, until recent publications of a series of pioneering studies aimed at filling the lack of knowledge in the sector. To this purpose, as compiled by Z. Chen *et al.* [51] various AM systems have been suggested and developed to optimize ceramic materials management. Moreover, by referring to R. Morales *et al.* review [50], many successful AM attempts have been carried out for the implementation of complex hierarchical microstructural and functional layers that improve the energy devices performances.

1.4.1. Extrusion

1.4.1.1. Fused Deposition Modelling

Fused Deposition Modelling (FDM) is the most common 3D printing techniques. It produces complex objects from molten wires of thermoplastic polymer or metal materials extruded through a nozzle. The material filament is continuously supplied via a pinch roller system and heated inside a movable nozzle at a temperature slightly higher than its melting point, such that it can be easily extruded through the nozzle to form layers. Upon extrusion, the material hardens above the previously printed layer and the supporting platform is lowered, so that the extrusion of the next layer can take place. Multiple parallel extruders can be used to incorporate different build materials and to lay a sacrificial material, to support overhanging structures of the object during the building process.

Low cost, high speed, flexible unit size and simplicity of the process are the main benefits of this technique although shrinkage problem after the post – treatments, layer – by – layer appearance, low resolution, poor surface quality and a reduced number of ceramic feedstock materials available, limit its applicability in a few sectors.

1.4.1.2. Robocasting

Robocasting (RC), also known as Direct Ink Writing (DIW), works almost in the same way as FDM, except that in this case concentrated suspension or colloidal gel of the material of interest is deposited at room temperature through a syringe type nozzle. Shape and structure retention when the inks flow out the nozzle is due to the rheological properties of the inks rather than solidification [52]. The deposition can be operated in continuous mode or Drop – On – Demand (DOD) mode and occasionally the plate can be heated to dry the deposited layer and maintain the wanted shape.

Ink rheology and ink preparation, typically formulated with fillers, binders, additives, and solvents [53], are the main parameters for ink printability and to avoid nozzle clogging. RC can be performed using commercially available fused deposition modelling 3D printers equipped with universal paste extruder [54] that provides the same advantages as FDM and reduces cracking and sample deformation caused by shrinkage problems.

1.4.2. Vat Photo – polymerization

1.4.2.1. Stereolithography

Stereolithography (SL) derives from the terms "stereo", which describes a three-dimensional process, and "lithography", which means the print of elevated or recessed structures on a flat surface [55]. This technique first proposed and developed by C. Hull in 1986 [47] and later commercialised by 3D Systems Inc., consists of the selective curing of a photosensitized monomer resin or solution contained in a vat, by using a light source typically in the ultraviolet range. Generally proceeding point-to-line, line-to-layer, then layer-by-layer, the monomers, mainly acrylic and epoxy-based, are light activated and instantly converted into polymer chains pattern (Polymerisation). When polymerisation is complete for one layer, the vat or platform supporting the work piece is lifted or lowered by the thickness of a layer, according on the building process mode. Afterwards, the next layer can be applied, although in some cases the photocurable liquid has to be smoothed by a wiper blade. By this method, the finished part must then be post-cured through heat-treatment or UV-irradiation of the entire surface.

SL is capable of printing well – defined architectures at a fine resolution, managing the energy of the light source, speed and time of exposure to the light in each layer. However, since the object is constructed in a vat filled with a specific resin, SL technique works with a single build material that limits its applicability in multi – component devices.

An extended method of stereolithography that enables a direct fabrication of 3D complex ceramic parts is called Ceramic Stereolithography (CSL). The CSL can be subdivided into direct CSL, in which well dispersed fine ceramics particles, surfactants and additives are incorporated into a photocurable medium, or Indirect CSL, where the photocuring liquid is cured and then used as a mould for ceramic casting. After the green body formation, typically debinding and pyrolysis, followed by high temperature sintering, are required to reach high density components. Ceramic suspension composition and light scattering arising from ceramic particles are the main challenging parameters of this technique.

1.4.3. Binder jetting

1.4.3.1. Three – dimensional printing

The Three – Dimensional Printing (3DP)[2] method produce components by distributing a liquid binder with a printer head on a layer of powder. The binder permeates into the powder layer, solidifies and encloses the surrounding powder. The build platform is subsequently lowered and a new layer of powder is distributed by a levelling roller over the previous one, repeating the construction process until the part is finalized. Afterwards, the workpiece undergoes de – powdering and sintering processes to remove the unprocessed powder and organic binders, respectively, giving the component the desired mechanical strength.

3DP is mostly used and commercialized for biocompatible ceramic scaffolds and casting moulds, due to its poor surface quality and difficult densification that require additional processes (i.e. infiltration) limiting its applicability for high performance ceramics.

1.4.4. Powder bed fusion

1.4.4.1. Selective Laser Sintering & Selective Laser Melting

The Selective Laser Sintering (SLS) is a selective sintering process of a powder bed by means of a high-power laser beam. The laser, hitting the dust bed in a control atmosphere, heats and partially fuses the surrounding particles together to form a layer. After finishing the first layer, the build platform is lowered by one-layer thickness. Thereafter, the powder is spread on the previous surface by a re - coater for the next heating and joining phase between particles and layers, until the 3D part designed is completed. As in the 3DP method, overhanging regions are supported by untreated powder, which means that no additional support is needed for the construction process. SLS is mostly used to produce high density metal alloy parts with complex shape and superior mechanical properties compared to conventional methods, in a process named Direct Metal Laser Sintering (DMLS) [56].

Considered a variant of the SLS, Selective Laser Melting (SLM) is a one-step technique to completely melt the powder bed using a high energy density laser. The high energy involved in this process makes it possible to produce pieces of complex shape with low porosity and controlled crystalline structure without further treatments.

[2] The term "3DP" is maintained for historical reasons to the single 3D printing technique, while "3D printing" is now a popular term which represents any additive manufacturing technology [51].

Fused Deposition Modelling (FDM)

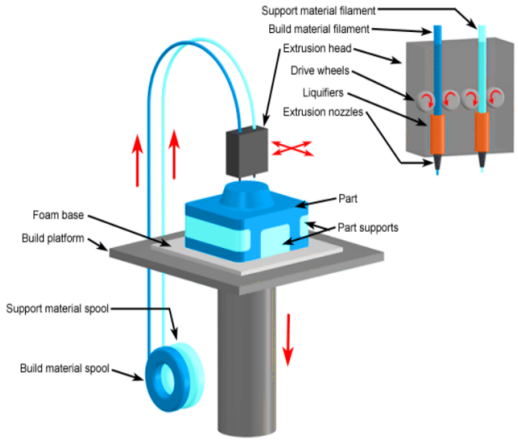

Feedstock

Thermoplastics filament with solid loading above 40% wt and grain size 1 – 5 μm

Power source

Thermal energy

Post treatments

D / S

Advantages

Cost effective methods; produce dense and porous structures after firing process; printed object easily removed.

Disadvantages

Poor mechanical properties of the printed parts; not good for small features, details and thin walls (layer thickness of 100 μm); stair – step effect; printing heads prone to clogging; filament processing.

Energy applications

Fabrication of micro-reactors (gas capture, gas separation, water purification, etc.); Solar concentrators; Components for solid oxide fuel cells.

Robocasting (RC)

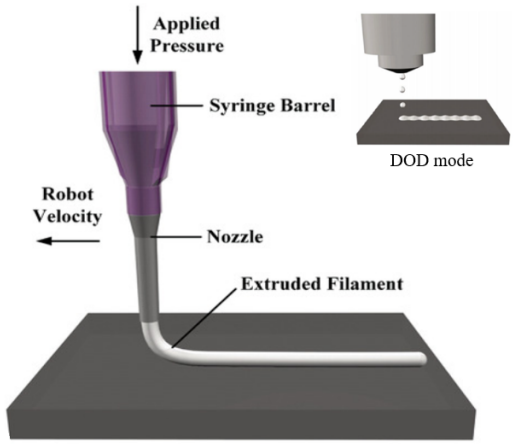

Feedstock

Concentrated suspensions or colloidal gel with solid concentration up to 60 vol% and grain size of 30 nm to 2 μm

Power source

Thermal energy

Post treatments

D / S

Advantages

Cost effective methods; produce dense and porous structures after firing process; printed object easily removed; wide range of materials

Disadvantages

Not good for small features, details and thin walls (layer thickness of 50 μm); stair – step effect; printing heads prone to clogging.

Energy applications

Components for SOFCs; components for batteries and capacitors; components for solar cells

Stereolithography (SL)

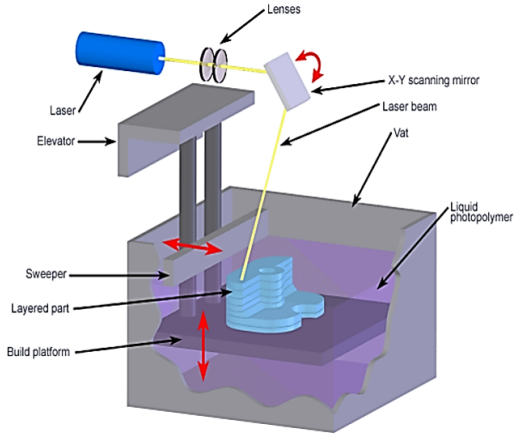

Feedstock

Highly viscous photocurable pastes with solid loading >50 vol% and grain size 0.5 – 5 μm

Power source

Laser

Post treatments

C.S. / D / S

Advantages

High vertical resolution (10 – 25 μm); high surface finish; porous or dense materials can be printed; ceramic pastes acts as integrated support structure; excellent mechanical properties of the printed

Disadvantages

Difficult no printed material reuse

Energy applications

Microcell concentration PV array; Fabrication of micro – reactors (gas capture, gas separator, water purification, etc.); Components for Solid Oxide Fuel Cells

Three – dimensional printing (3DP)

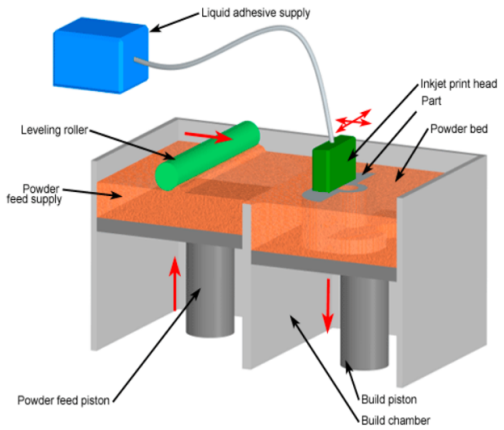

Feedstock

Inorganic powders with grain size around 50 μm

Power source

[-]

Post treatments

DPw. / D / S

Advantages

Powder acts as integrated support structure; high printing velocity.

Disadvantages

No printed material can be reused; finishing depends on powder grains size, poor mechanical properties of the printed parts; low resolution up to 100 μm

Energy applications

Fabrication of micro-reactors (gas capture, gas separation, water purification, etc.).

Selective Laser Sintering (SLS) & Selective Laser Melting (SLM)

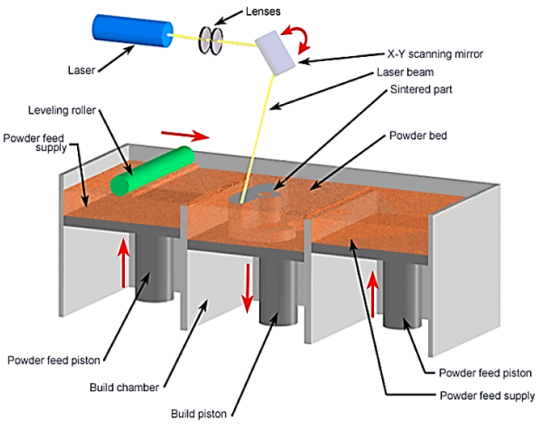

Feedstock

Low – to – High melting temperature metals in powder form, grain size 0.3 – 10 μm

Power source

Laser

Post treatments

D / S (SLS only)

Advantages

High mechanical stability; powder acts as integrated support structure; good mechanical properties of the printed parts.

Disadvantages

No printed material can be reused; expensive equipment; low speed; layer thickness of 100 μm; finishing is dependent on powder grain

Energy applications

Metal-supporting layer for SOFCs and metallic membranes; Fabrication of complex metallic microreactors

Legend: D= debinding; S=sintering; C.S: Cleaning Samples; DPw: De-powdering

Table 2| AM systems characteristics and energy applications with references [50] [51] [52] [55] [57] [58] [59] [60]

1.5. Outline of the thesis

This MSc project has been carried out at *"Institut de Recerca en Energia de Catalunya (IREC)"* (Barcelona), Research & Development company leading scientific and technological progress and advancement in the field of energy [61]. Materials and equipment were obtained through the project" BASE 3D: Agrupació en tecnologies emergents en fabricació additiva-WP2:3D-LIGHT - Code: 001-P-001646".

The manuscript involves the utilization of different fabrication and characterization techniques for producing SOCs by means of Stereolithography.

The experimental part (Chapter 2) provides information about the set-up and techniques utilised, such as the printing process or the functionalisation by infiltration.

Chapter 3 entitled "fabrication and design" gives technical details about the structures of electrolyte supported devices made of 3YSZ by SL and the results of the fabrication process. Two different kinds of configuration are considered: planar design, and spiral design. The fabrication process is described in detail, considering possible design, the printing process, the cleaning and the sintering of the pieces after printing.

Afterwards, in Chapter 4 the manuscript describes the functionalization process of the cells. Different inks where formulated and characterized to fabricate the electrodes of the SOC devices. The different anode slurries were characterized with printability test, rheological measurements and fluidity test, in order to find the best optimization to functionalize the cell with these innovative designs. Commercial LSM-YSZ inks were deposited on large area cells with planar design. NiO-YSZ based inks were printed on dummy samples and inside a complete spiral, sintered at high temperature and observed by scanning electrode microscope (SEM). The good microstructure observed by SEM confirmed the feasibility of the electrodes fabricated for application in SOC technology.

The last part of the work, shown in chapter 5, involves the electrochemical characterization made to evaluate the performance of the device fabricated for a future application in real devices. In addition is highlighted the potential of the 3D printed parts for functional ceramics.

Chapter 2| Experimental methods

2.1 Fabrication Technique: Stereolithography (SLA)

2.1.1 The SLA printing process initialization

As briefly introduced in chapter 1, stereolithography consists of selective polymerization of photo-sensible resin, by a light source. Photo-polymerization is the chemical reaction to link molecules (monomer) into larger ones (polymers) [62] that requires an activation energy provided through light irradiation. Generally, the resin formulation consists of monomers and oligomers to form the polymeric structure, photo-initiators that convert incident light into chemical energy in the form of reactive intermediates (radical formation), photosensitisers to shift the light absorption of photo-initiators to desired wavelengths, and additives to improve solubility or to adjust the resin viscosity. Here the paste used to build 3D parts was the commercial 3YSZ paste with particle size 0.1-0.8 μm (80%wt solid load) by "3D CERAM".

3D printing process starts with the design of a CAD model. In this work, the CAD model has been built using "*SOLIDWORKS*", following certain design frames dictated by the printing process, cleaning, and heat treatments. First, the CAD model must be designed without exceeding a well-defined maximum wall thickness to avoid piece failures due to cracks caused by internal stresses during debinding. Likewise, rounded shapes have better chances of success than sharp edges and pieces need to be designed without closed cavities or long thin and blind holes. Furthermore, during design for 3D printing, it is fundamental to think about the printing direction, as the part is built layer by layer from the bottom to top, it is more appropriate avoid any additional support which leads to unnecessary and expensive print comparing to a self-supported piece. In this regard, the component could be designed with modified shape to support the overall structure or adding an additional support to remove manually after debinding. The presence of a support depends on the piece geometry and the printing material. Since solid oxide electrolyte printing requires a high viscosity paste due to the high solids load, projecting structures can be supported without direct contact with the support. It is possible to place a thin layer of paste at a certain distance between the support and the part to counteract scraping stress.

Once the CAD designing was completed, the model was exported as an STL file. This file was then computed through "*Materialise Magics*", which allows to virtually allocate the pieces on the building platform, to perform Z compensation, piece rescaling (to accommodate for heat treatment 1.245 on the length, 1.246 on the width and 1.267 on the thickness) and mesh errors correction. The build plate positioning (figure 9) includes the piece orientation which has been chosen to set with membranes along the scraping direction (x axis), to avoid scraping stresses which may lead to print failure. The Z-compensation, the adjustment in the component height positioning to take into consideration the polymerization depth being greater than one layer in slopes or overhangs, was set 100 μm.

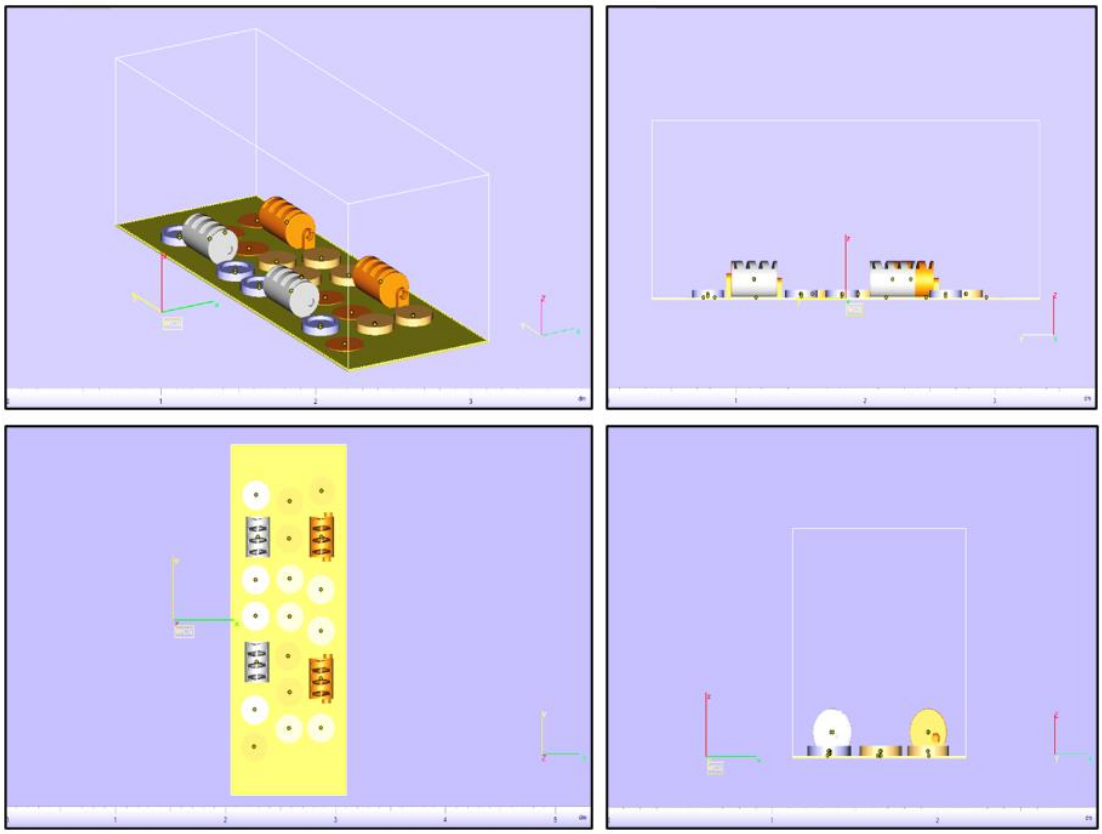

Figure 9| Materialise magic layout during the STL file preparation.

The STL file is then imported into the printer's control software Direct Machine Control (DMC), where the part visually appears on the screen in the defined workspace and a preview of the printing process can be carried out, as shown in figure 10 and figure 11. As each paste has specific setting files, the user needs to select the appropriate scraping parameters such as scraping speed, layer height and laser parameters including cured thickness, hatch and contour offset, hatch angle between layers, beam speed and power.

In the section "*actions*" of the settings parameters shown in figure 12, were uploaded the scraping parameters before printing and before each slide. This subdivision is due to the fact that as the printing starts, a sufficient amount of paste must be spread to have a very resin flat plane and avoid hollows, while the scraping before each slide spreads the desired thickness of resin to be hardened (100 μm). Furthermore, slicing distance was set to define the curing thickness of each layer, in which 25 μm is the minimum thickness dimension of the machine, which affect the resolution of the component. Furthermore, due to each layer is greater than the slice set, to give sufficient adhesion between the processed layer and the previous one, the hatching angle, which defines the curing of a slice constituting the layer was defined firstly in horizontal direction and afterwards in in the direction shifted of 90° to reduce internal stresses generated during the polymerisation process.

As shown in figure 13, in "*hatching & marking"* parameters were defined the pattern, spacing between cured lines and sequence of the hatching curing process, the triggering frequency and curing speed. The hatching curing occurred first then marking process to avoid piece distortion and internal stresses. In this section was also defined the percentage of laser diode current which, strictly correlated to the laser power, allows to calibrate the power during the polymerisation test.

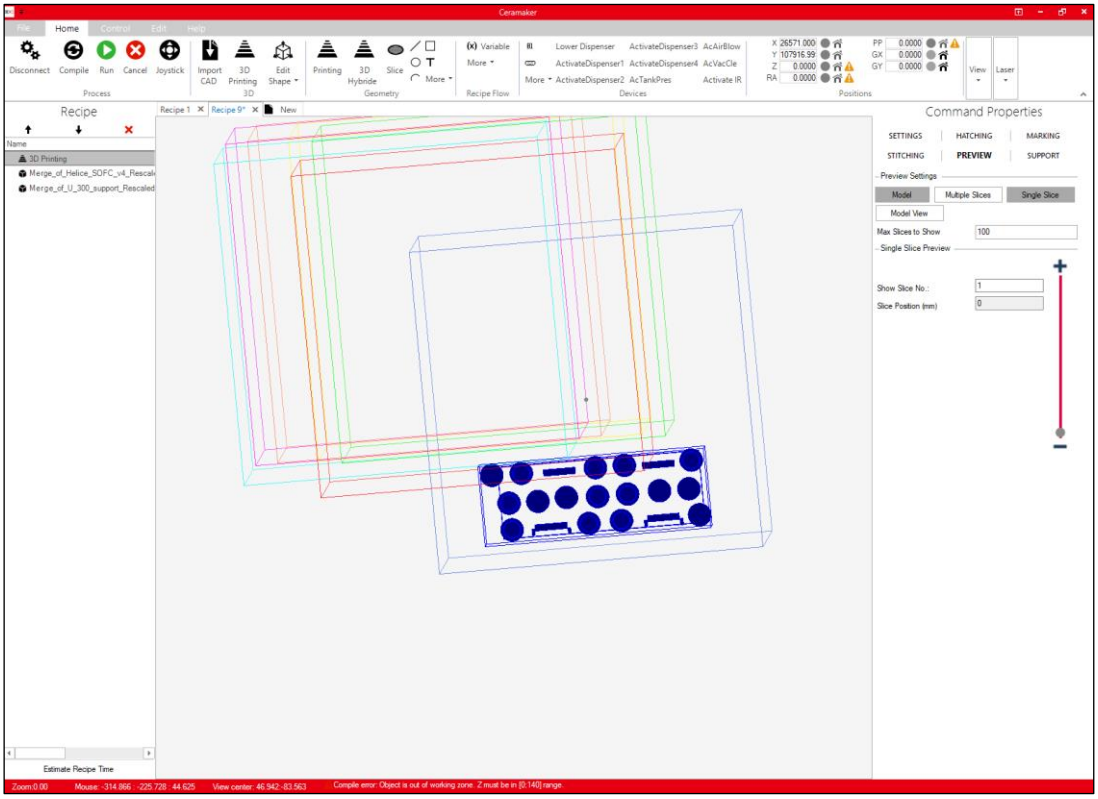

Figure 10| Printer control panel layout where is shown the SL platform representation in the working area (blue square)

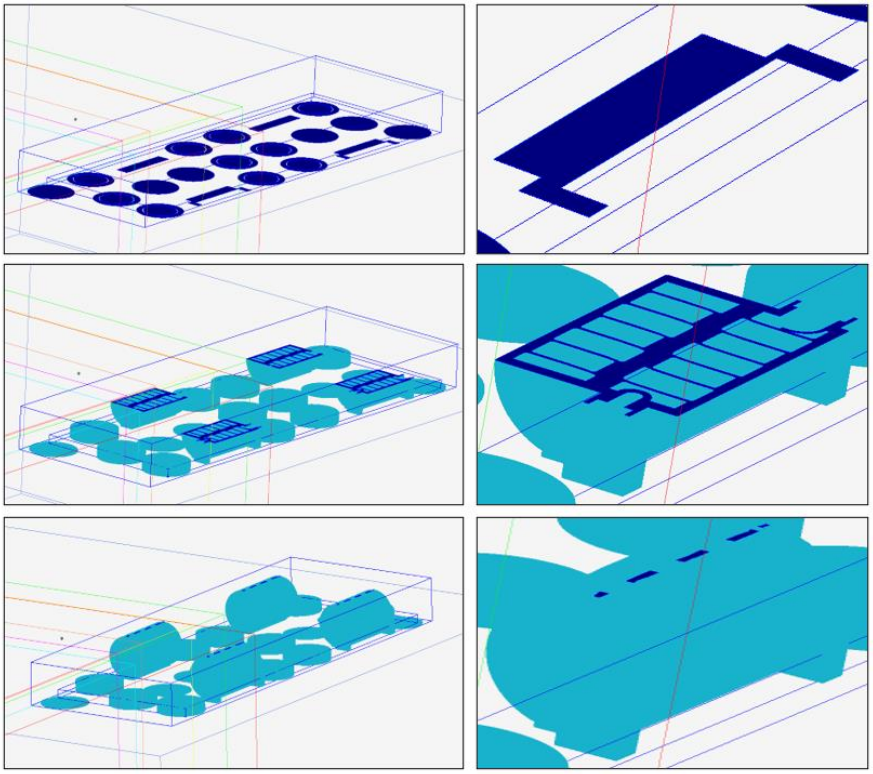

Figure 11| SL printing process preview with magnification of the spiral building sequence.

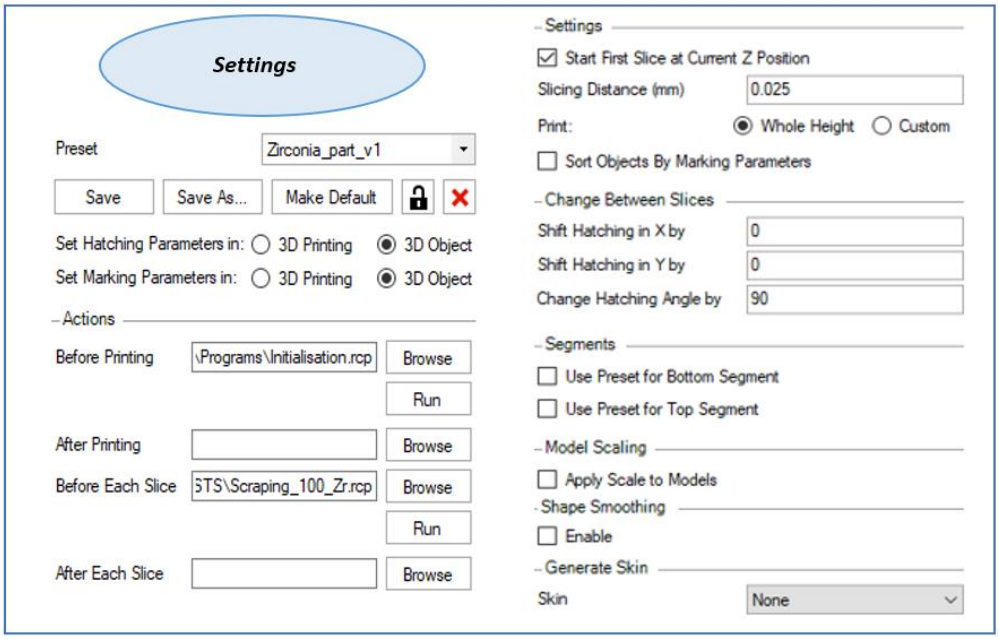

Figure 12| Settings parameters. Scraping parameters and slicing distance were uploaded.

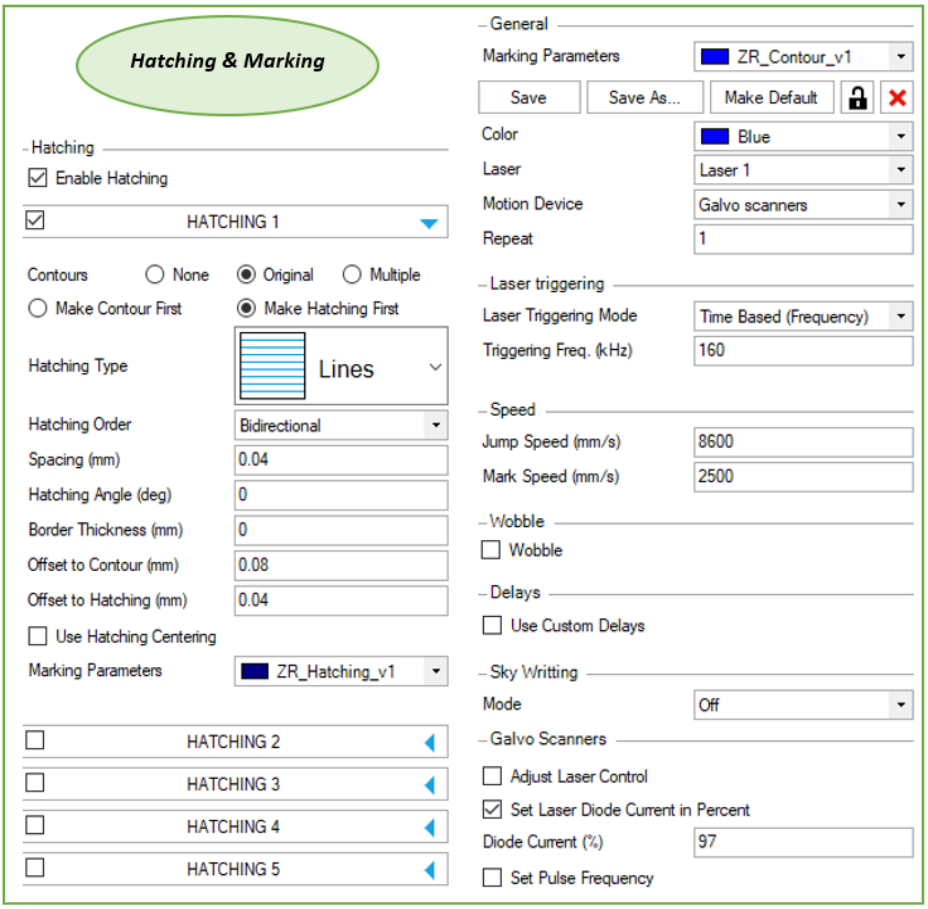

Figure 13| Hatching & marking parameters. Scanning pattern, spacing between cured lines and hatching sequence of the triggering frequency, curing speed and percentage of laser diode current were set.

2.1.2 Doctor blade: CERAMAKER

The SL doctor blade machine, named CERAMAKER by the developers at *3D CERAM*, is an experimental prototype machine. This machine combines the SL and robocasting[3] processes with the goal of printing cells in one single step. The SL technique is suitable to print dense structure for the electrolyte while robocasting deposits slurry suitable for electrodes fabrication. To this regard, the robocasting apparatus is equipped with four nozzles to deposit for different materials, an infrared laser to cure the slurry and a blower to remove material such as the uncured paste. The SL apparatus is composed of five subsystems (highlighted in figure 14) to work properly and ensure the part building.

The first subsystem is the recoating system which supply a new layer of uncured resin on the surface of the vat by using two recoater blades[4]. The first blade is used for spreading the paste, whereas the second blade to set the printing layer. The second subsystem is the Vat system including the resin tank and a level adjustment device. The laser & optics system to scan the laser beam across the resin surface and cure it. This system consists of a laser beam generator, focusing and adjustment optics, a UV filter and a galvanometer scanning head. The UV laser from the *Innolas* company (nanio) uses an IR diode as pump for a Nd: YAG crystal follow by two frequency multiplying crystals to reach UV emission at 355 nm. The fourth and fifth subsystems are the platform system which is composed of the set of built platform and elevator, and the control system. The control system manages the machine sequences operations executing the operations described in the STL file, actuating the beam controller which deals with modifying beam spot size, focus depth and scan speed, or adjusting the resin level and changing the vat height, detected by sensors used also to avoid blade crashes.

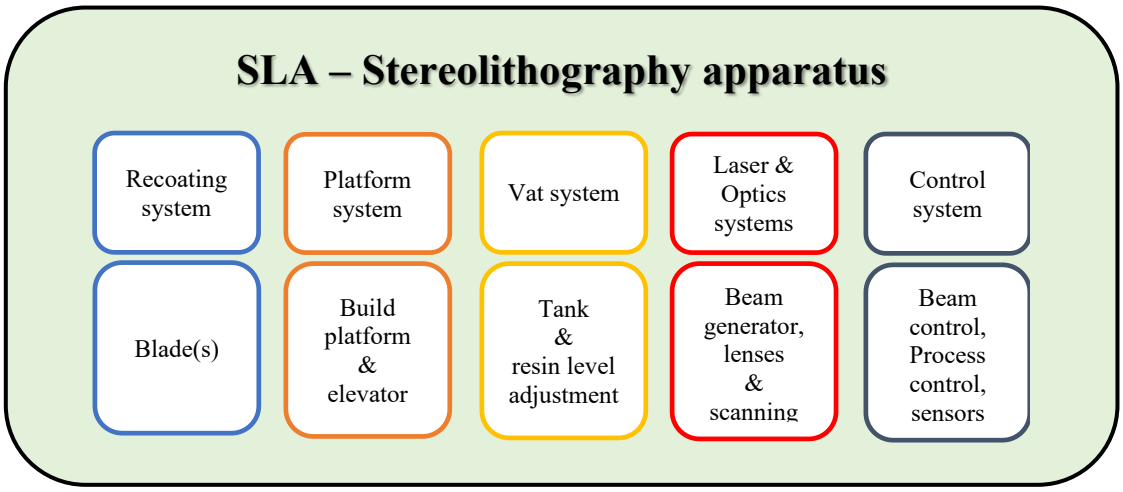

Figure 14|Stereolithography apparatus composed by 5 sub-system: recoating, platform, vat, laser & optics and control system.

[3] Note that hybrid printing is not the subject of this work as only the stereolithography technique was used.
[4] Also referred to us as doctor blades.

CERAMAKER

- **Dimension**: 1000 x 2200 x 1900 mm (WxDxH)
- **Printable size:** 300 x 300 (adjustable) x 100 mm
- **Weigth:** about 1450 kg
- **Electrical requirements:** 220-240 VAC/50 Hz – 2000 W
- **Room operating temperature:** 20-25 °C
- **Room maximum temperature variation:** 1°C/hour
- **Relative humidity:** 50% if possible
- **Laser**
  - **Type:** Semiconductor laser
  - **Light source:** UV laser
  - **Wavelength:** 355 nm
  - **Power:** 1.3 W
- **Recoating**
  - **Process:** scraping
  - **Blades:** 2
  - **Layer thickness** min: 0.010 mm
  - **Layer thickness** max: 0.125 mm
- **Optical & scanning**
  - **Beam diameter:** about 10 um
  - **Beam speed:** 5000 mm/sec
- **Drawing speed:** (Z direction). 20 – 200 layers per hour*.
- **Tank max capacity:** 280 x 120 x 130 mm (WxDxH)

*50 layers per hours optimal with optimal conditions. Ceramic printing speed highly depend on what need to be printing. Printing time is the combination of the lasering time (surface to be lasered) and time for the recoating blade to cover the working area (length).

Figure 15 | 3D CERAM Hybrid SLA & Robocasting at IREC facilities. Technical data of the printer released by 3D ceram.

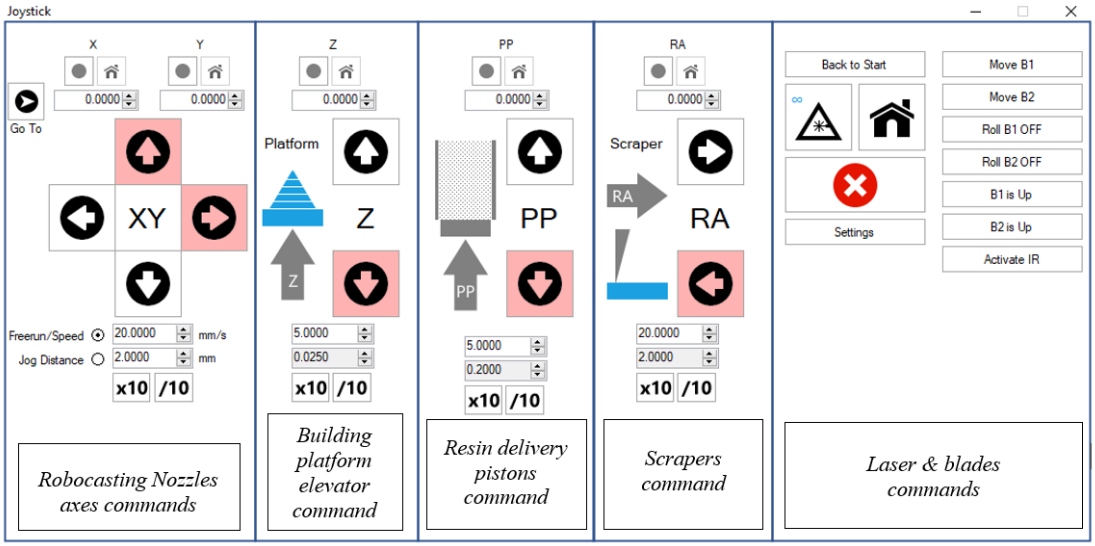

Figure 16 | Printer Joystick representation. The joystick allows to manage the laser, building platform system and robocasting nozzles position.

The printer set-up started with the build plate preparation, which consisted in placing a magnetic paper and a grip layer on top of it, to prevent building platform sliding and to increase the print attachment. It is essential at this stage to prevent protruding edges or other material interfering with the blade's recoating procedure later on.

Once the platform was ready, the blades were properly cleaned, installed and adjusted in height from the building platform by means of shims corresponding to the desired scraping heights. In particular, the blade gap, distance bottom of blade and resin surface, was set 150 μm for the blade 2 and 50 μm for blade 1.

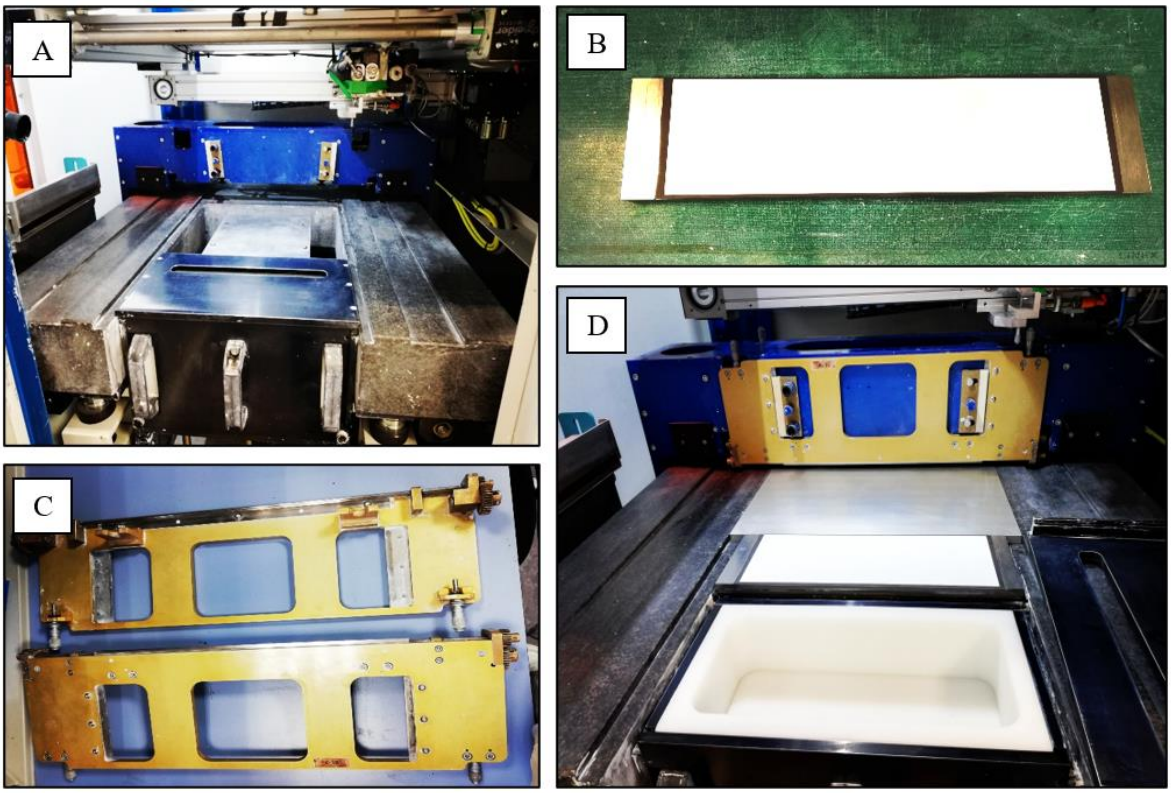

Figure 17 | Printer set-up where figure A shows the machine ready for the installation of blades (figure C) and building platform (figure B) with magnetic layer (grey) and adhesion-enhancing layer (white). In figure D is shown the machine after the blades and building platform installation and the empty paste tank.

The tank was filled with the paste, pushed out through the resin delivery system by pistons and a preliminary coating was accomplished onto the building platform. Before to start the printing process, a polymerisation test was required to calibrate the laser power in order to achieve the desired cured thickness of four to five times the layer height. This test involves irradiating a flat area of uncured paste and measure its polymerized thickness with a micrometre. If the thickness results thinner than the desired one, the power must be increased and vice-versa. After the curing test has been completed, the printer was ready to start.

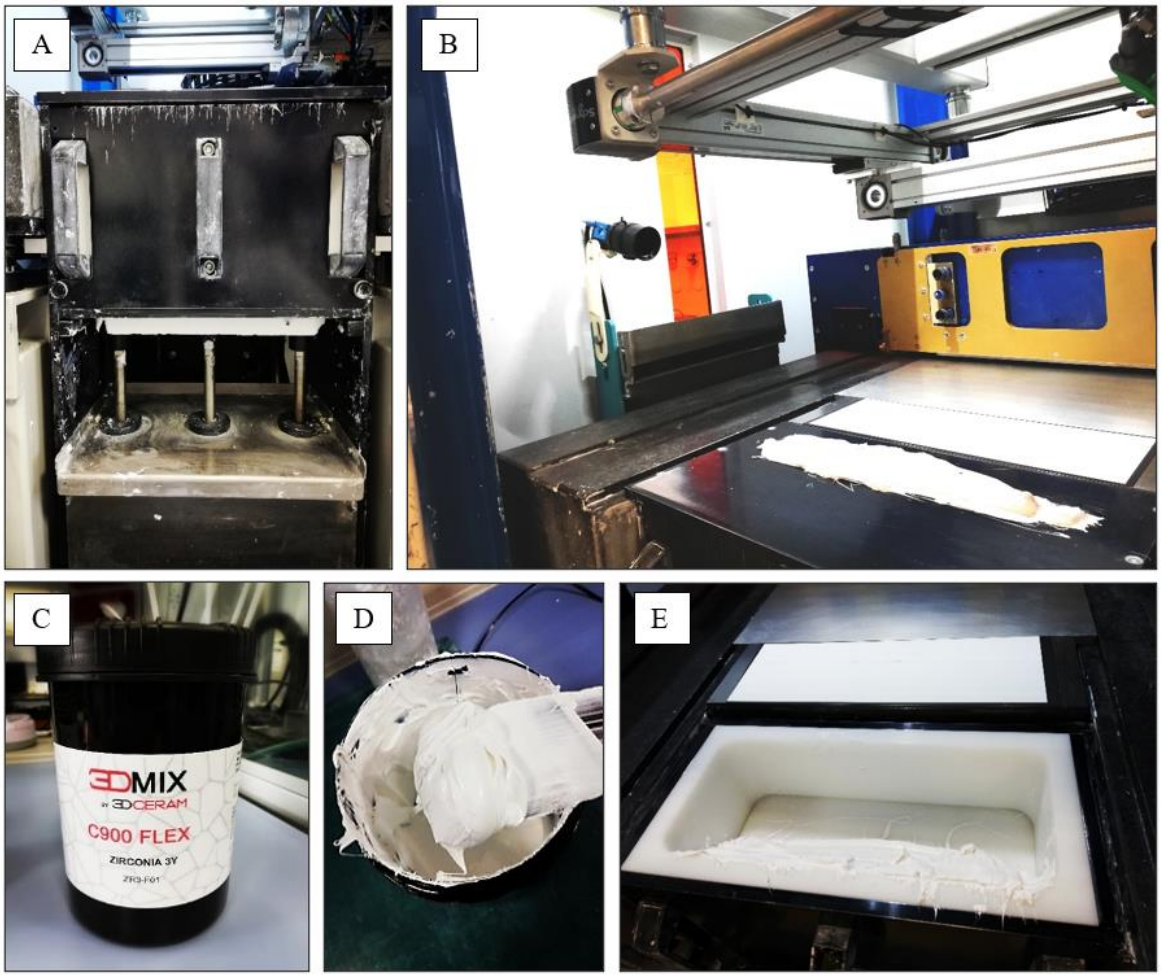

Figure 18 | Representation of tank filling (figure E) with commercial 3YSZ paste (figure C), material adopted to print the tubular cell with spiral design and large cell area. As figure D shows, the 3YSZ paste for SL printing result very dense, shine and viscous, due to the high solid loading (80% wt). Figure A highlights the tank with the three pistons that raise the base of the tank in order to adjust the resin level. Figure B shows the final set-up and the side camera for remote control of the printing process.

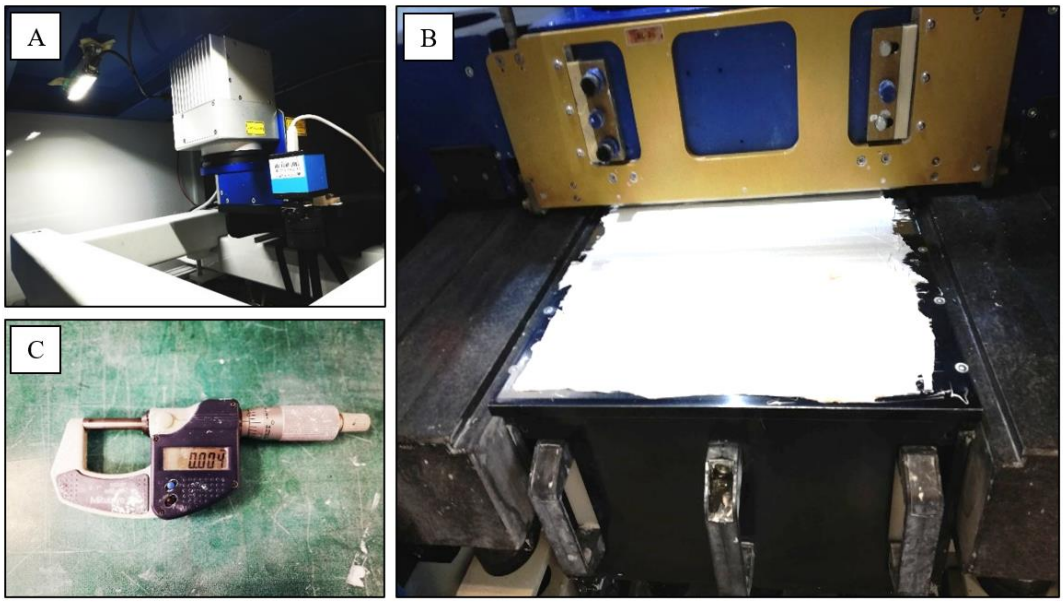

Figure 19 | Polymerisation test preparation. Figure A shows the laser & optics system, while figure B and C show the paste levelling for polymerisation test and the micrometre, respectively.

2.1.3 The resin printer: Formlabs Form 2

Based on SL printing process, this printer made by *"Formlabs"* was used to print with resin without solid load the tool to evaluate inks fluidity and some spirals. As described before, also in this case the printing process starts form the CAD model transferred in STL file for the subsequent configuration of the printer. Like every SL printer, this device also has subsystems such as tank and resin supply, UV laser system and control system. On the contrary of the *Ceramaker* printer, the curing approach occurred through a bottom-top approach of laser system. The printing procedure consisted of manual filling of the tank in the range defined by two level indicator lines followed by automatic platform plunging inside the resin, which position regarding the bottom of the resin tank defines the layer thickness. As the uncured material was liquid, the building parts mostly needed a support to be removed after the printing, an example is shown in figure 20 for a custom air blower fabrication for the *Ceramaker*.

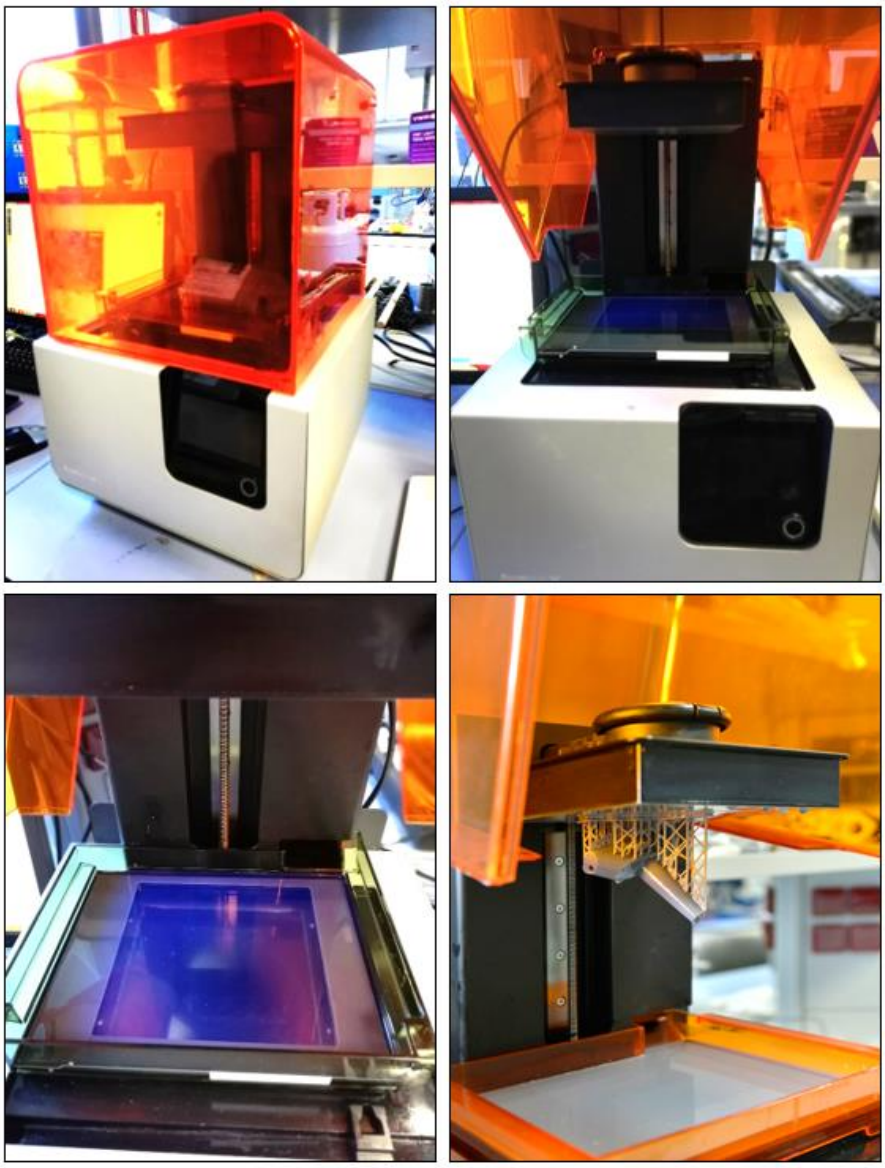

Figure 20 | The Formalabs resin printer at IREC facilities

2.2 Inks preparation

2.2.1 Ink for the anode of spiral design

NiO/YSZ inks were prepared to functionalize by injection the inner chamber of the SOC spiral design. All the inks formulation in this section contains about 28% vol. of solid load, 14 % vol of which is the ceramic compound. Three types of inks have been prepared to find the best properties regarding open porosity and surface wettability. The ink composition consists of a solvent as a base for the other compounds: a binder, two type of pore formers, and the ceramic powder. While the binder retains other colloidal, the dispersant stabilizes the colloidal suspension to avoid agglomeration and to provide ink homogeneity. The colloidal stability of the system could be achieved electrostatically by enhancing the electrostatic inter-particles interaction and reducing the Van Der Waals forces. Another strategy is the utilization of steric repulsion, here a polymer is attached to the particles surface avoiding the formation of aggregates. Very often the combination of both strategies is used (electro-sterically). Regarding the pore formers, these are materials of different shapes and dimensions which burn during the sintering process, leaving place to an open porosity. In this work two kinds of pore formers have been used: spherical *Poly-methyl methacrylate* (PMMA) particles of 1.5 µm of diameter and graphite platelets of average diameter 44 µm, respectively. The choice of the two different kind of pore formers was done with the aim to obtain an interconnected porosity.

Figure 21 | Ball miller and Zirconia balls at IREC facilities. By placing the solution and a couple of zirconia balls in a container, the solution was mixed on the rollers for 1 day.

The mixing process was carried out in a planetary miller (Figure 21). The suspension was mixed for 5 minutes after the addition of each components. With the aim to reduce agglomeration the inks were put for 10 minutes in an ultrasonic bath afterwards. Finally, the inks were mixed for 20 minutes in the planetary miller to ensure good homogeneity.

Figure 22 | Planetary miller at IREC facilities

The first ink (I1) was prepared by first mixing the *Propylene Glycol (PG)* from *Sigma Aldrich* with two types of *Polyvinylpyrrolidone (PVP) (Sigma Aldrich)*, K30 as dispersant and K90 as a binder. Then, to reduce the agglomeration of K90, 10 minutes of sonication were performed on the ultrasound bath. The commercially available NiO-YSZ powder (60-40 wt%) with particle size about 0.6 μm from *Kceracell* was then added, followed by *Polymethyl Methacrylate (PMMA) (Sigma Aldrich)* to obtain a close porosity of ≈ 1,5 µm in diameter and the commercial graphite flakes from *Alfa Aesar* with platelet shapes (44 µm diameter).

The second ink (I2) is made by first mixing the PG and K30 (95%-5% vol) in a ball miller for 1 day. Afterwards additional solvent is added to reach the same dispersant concentration as for ink 1. Finally, the NIO / YSZ powder, PMMA and graphite are incorporated. For this ink, the addition of binder is avoided to maintain low viscosity.

The third (I3) was based on the second ink with the addition of *Triton 100 (Sigma Aldrich*) as surfactant.

I1			**Amount (g)**	**Amount (ml)**	**Amount (g%)**	**Amount (ml%)**	**Density (g/ml)**
Solvent	PG		14	13.46	38.6%	69.8%	1.04
Binder & Dispersant	PVP	K30	0.34	0.28	0.9%	1.5%	1.2
		K90	0.25	0.21	0.7%	1.1%	1.2
Ceramic load	Ni-YSZ		17.1	2.65	47.1%	13.8%	6.442
Pore formers	PMMA 1.5 μm		1.6	1.33	4.4%	6.9%	1.2
	Graphite 44 μm		3	1.35	8.3%	7.0%	2.23
	TOT		36.29	19.29	100%	100%	

I2		**Amount (g)**	**Amount (ml)**	**Amount (g%)**	**Amount (ml%)**	**Density (g/ml)**
Solvent	PG	7.3	7.02	20.4%	36.9%	1.04
Dispersant solution	PG-K30	6.8	6.67	19.0%	35.1%	1.04
Ceramic load	Ni-YSZ	17.1	2.65	47.8%	14.0%	6.442
Pore formers	PMMA 1.5 μm	1.6	1.33	4.5%	7.0%	1.2
	Graphite 44 μm	3	1.35	8.4%	7.1%	2.23
	TOT	35.8	19.02	100%	100%	

I3		Amount (g)	Amount (ml)	Amount (g%)	Amount (ml%)	Density (g/ml)
Solvent	PG	7.1	6.83	19.74%	35.87%	1.04
Dispersant solution	PG-K30	6.8	6.54	18.91%	34.35%	1.04
Surfactant	Triton 100	0.36	0.34	1.01%	1.77%	1.07
Ceramic load	Ni-YSZ	17.1	2.65	47.79%	13.95%	6.442
Pore formers	PMMA 1.5 μm	1.6	1.33	4.45%	7.00%	1.2
	Graphite 44 μm	3	1.35	8.34%	7.07%	2.23
	TOT	35.96	19.03	100%	100%	

Table 3| Inks recipe composition. In the tables are shown the recipes of the NiO/YSZ inks prepared to functionalize the inner chamber of the spiral cell.

2.2.2 Inks for the roughness promoter layer & cathode

The roughness promoted layer was sprayed by airbrushing to the 3YSZ electrolyte with the aim to enhance electrode adhesion. This 3YSZ ink is composed of 10 ml of ethanol, 1 g of 3YSZ powder (*Kceracell,* particle size of 1-10 μm) and 0,1 g of PVP - K30. The mixture was stirred for 24h. The slurry is further homogenised in the ultrasound bath stirred for 24h. The slurry is further homogenised on the ultrasound bath. It should be noted that this ink has a low solid load in order to achieve good spraying without blocking the airbrush.

The LSM-YSZ ink for the cathode deposition was prepared in a similar fashion, mixing 5 ml of ethanol, 0,005g of PVP – K30 and 0,5g of the commercial ceramic LSM-YSZ powder (0,4 μm) from *Kceracell.*

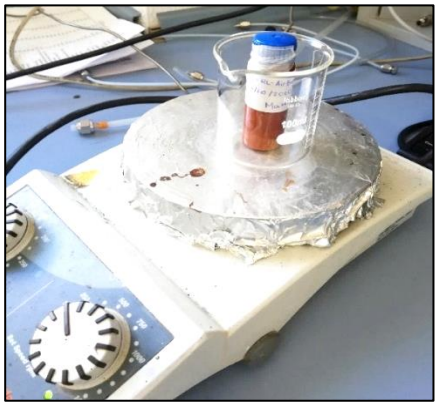

Figure 23|Magnetic stirring of roughness promoter layer ink.

2.3 Deposition Techniques

2.3.1 Injection of anode slurry

The anode slurry deposition was performed by manual injection with a syringe into the plastic as well as the ceramic spirals. The plastic spiral injection test aimed to evaluate effectiveness of ink deposition. As shown in figure 25, it consists of injecting the ink into one of the spiral anode chamber inlet/outlet, manually spin and gently shake the piece. Process is then repeated through the other inlet/outlet.

Figure 24| Syringe for anode slurry injection

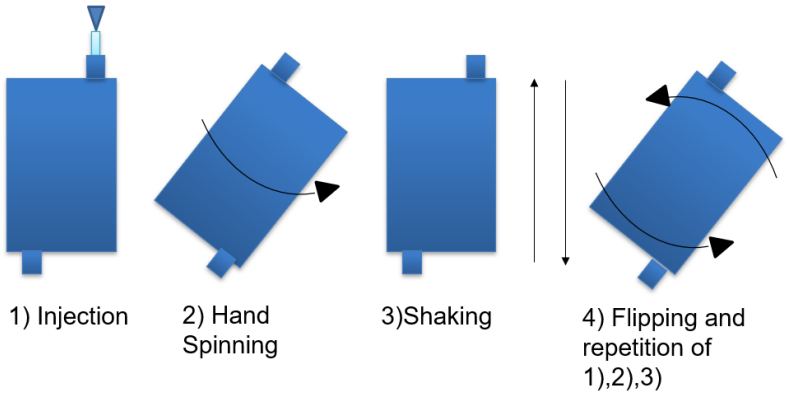

Figure 25| Injection of anode slurry procedure

2.3.2 Airbrush

This aerograph deposition machine consists of a standard and commercially available airbrush actuated by a 3-axis Prusa i3 style robot, shown in figure 26. The 3YSZ electrolyte was placed on the heat-bed at 50°C and non-desired area was masked with parafilm. The roughness layer was deposited spraying the mixture at constant height with a forward/backward movement. The deposition was left to dry in atmosphere. This process was repeated as many times as needed front and back. A thermal treatment follows at a heating rate of 2°C/min and reaching the dwelling temperature of 1200°C for 2h hours.

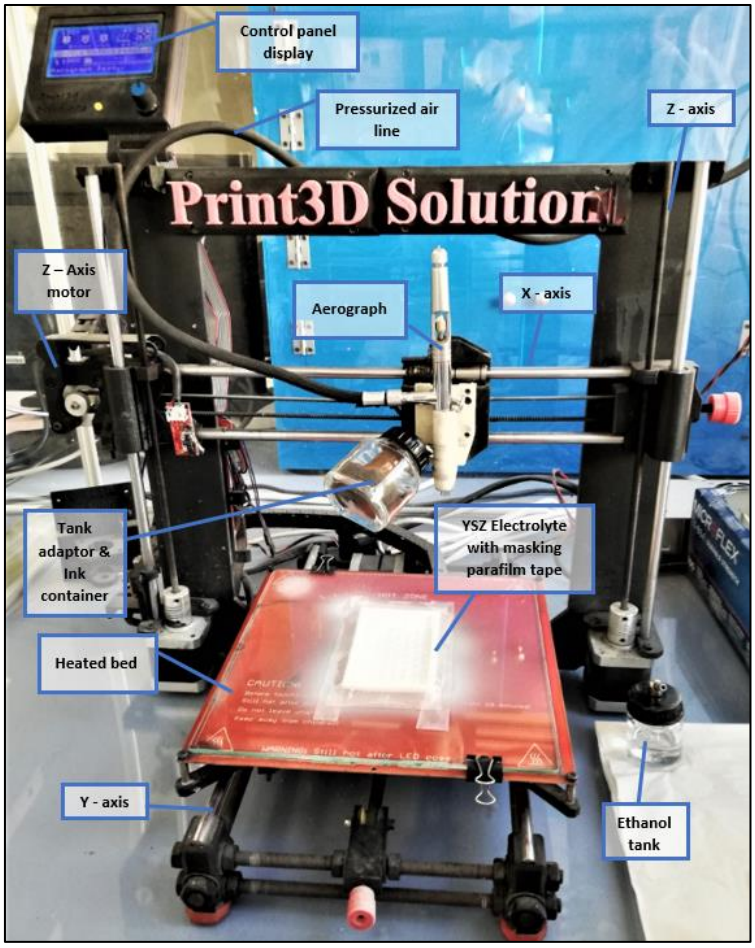

Figure 26 | Airbrush machine at IREC facilities

2.4 Rheological characterization for injection evaluation

2.4.1 Viscosimeter

Viscosity is a measure of a fluid's resistance to flow, under the application of a force. Viscosity can be quantified as the ratio of the shear stress, forces field parallel to the creep plane, and the shear rate, the rate of change in the speed at which a layer of fluid passes through an adjacent layer. By using a viscosimeter, it is possible measure the rheological properties of a fluid.

When the shear stress is proportional to the shear rate (or the viscosity is constant compared to the shear rate); the fluid can be classified as Newtonian. On the contrary, if the shear rate is a non-linear function of the shear rate (i.e., viscosity changes) by varying the shear rate, the fluid is classified as non-Newtonian. Non-Newtonian fluids can have four types of rheological behaviours: pseudo-plastic, plastic, Bingham, dilatant. The relationship shear stress – shear rate it is shown in figure 27.

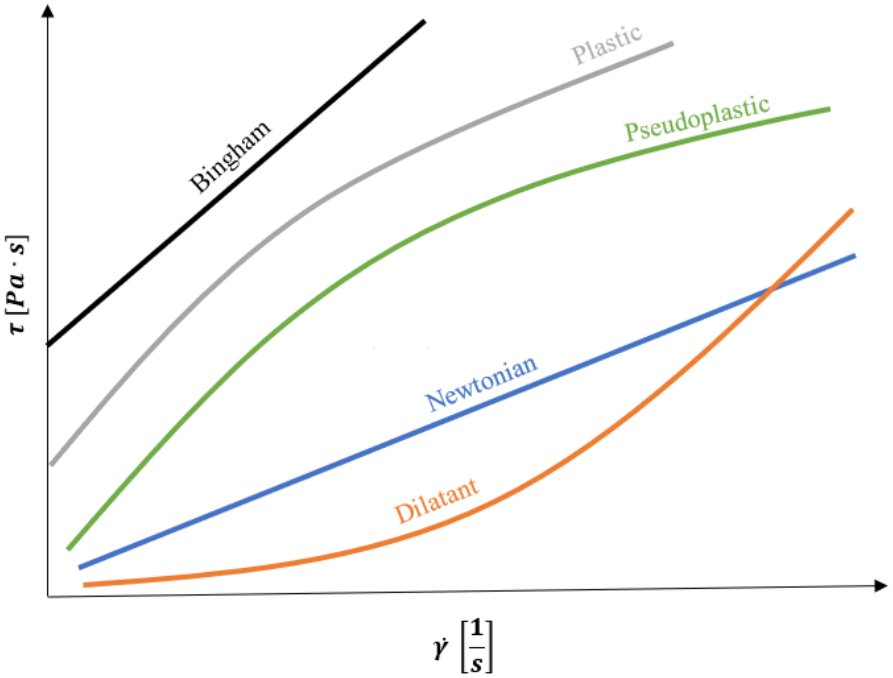

Figure 27| Rheological behaviour of fluids on the shear stress(τ) – shear rate ($\dot{\gamma}$) plane.

There are different commercially available types of viscometers which, according to their operating principle and geometry, are specific for different ranges of viscosity. As an example, rotational viscosimeters have the advantage of high flexibility and they are subdivided in coaxial cylinders, parallel plates and slab-cone (see figure 28). The larger the contact area, the better the viscometer is for measuring low viscosity liquids, indeed while coaxial cylinder type is suitable to measure low viscosity fluid (large rotor surface), parallel plates and slab-cone are appropriate to characterize viscous fluids. In this case, to characterise the anode inks was adopted the slab-cone (CP5°/30) rotational viscosimeter *Bohlin Visco 88* shown in figure 29. By using a gap slab-cone about 0.15 mm and placing enough ink on the plate (0.7 ml), viscosity, shear stress and shear rate were measured on the whole range of velocity (between 1 and 8).

Figure 28| Types of rotational viscosimeters. The figure represents the parallel plates, slab-cone and coaxial cylinders set-up.

Figure 29| Slab-cone rotational viscometer Bohlin Visco 88 *at IREC facilities. By changing the eight velocities from the slower (1) to the faster (8), the viscosimeter defines viscosity and shear stress of the fluid according to the shear rate.*

2.4.2 Fluidity Test

The fluidity test was carried out to choose the best ink surface tension for spiral injection goals. Viscosity is an important parameter to characterize the rheological properties of a fluid, but it is also necessary to take into consideration the interaction fluid-substrate. Ink fluidity was characterized through the dual flow fluidity tester [63] (figure 30) that was printed at IREC facilities with the *Formlabs* printer. The tool consists of a 13.5 cm high structure with two runway inclination levels (40° and 70°), where a tile of substrate could be placed. On the top of the runway there are two reservoirs with a capacity about 2.5 ml. With this tool, an equal amount of ink is placed in the two tanks and its drop was analysed along the 3YSZ 70° sloped substrate. The parameters measured are wetted path length and sliding time.

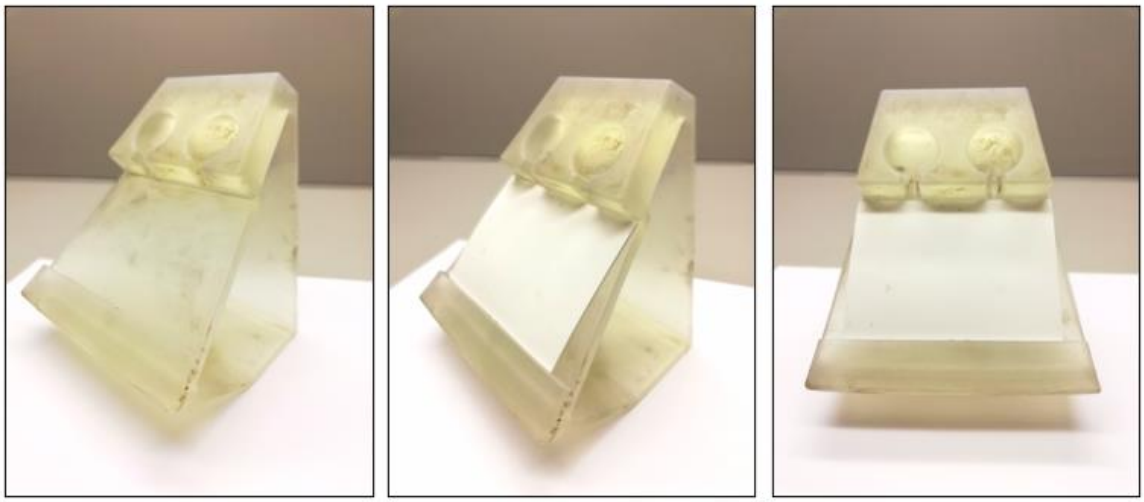

Figure 30 | Tool printed at IREC facilities using FORMLABS Form2 printer for measuring inks fluidity - [63].

2.5 Furnaces for thermal treatments and EIS

Debinding and sintering treatments were carried out for 3D printed parts and electrodes inks. The furnace for the thermal treatment of 3D printed parts was the *Hobersal* tubular furnace with ceramic bar heaters and maximum temperature of 1600°C. This furnace, shown in figure 31, is composed of an alumina tube bed contained in an insulator chamber and closed at both ends by two hermetic manifolds. The inlet end of the alumina tube is supplied by two *Bronkhorst* mass flow meters (for N2 and synthetic air) with maximum capacity of 1L/min. The outlet is connected to a bubbler to condense residues.

The *Lenton* furnace used for electrodes and EIS measurements, essentially consists of an insulated chamber with radiative coils and a thermocouple to sense the temperature of the chamber. The furnace can reach a maximum temperature of 1500ºC.

Figure 31| Hobersal *tubular furnace at IREC facilities for debinding and sintering process of 3YSZ.*

2.6 Debinding and sintering process of NiO/YSZ anode and LSM cathode

The heat treatment of the NiO/YSZ anode slurry was performed in an oven shown in figure 32. In this case, the removal of the binder is done by simple evaporation under atmosphere (without gas flow). The thermal treatment consists in drying the anode ink for 1 hour at 50 °C with a heating rate of 1 °C / min, and then sintering for 5 hours to the target temperature of 1250 °C with a heating rate of 1 °C / min.

Figure 32| Oven for thermal treatments at IREC facilities.

Since large cell cathode ink was dried for 1 hour on a hot plate at the temperature of 50 °C, the thermal treatment of LSM/YSZ consist of heating up to the sintering temperature of 1100 °C with a heating rate of 2 °C/min and maintaining a 2-hour dwell. The thermal treatments of the electrodes are highlighted in figure 33.

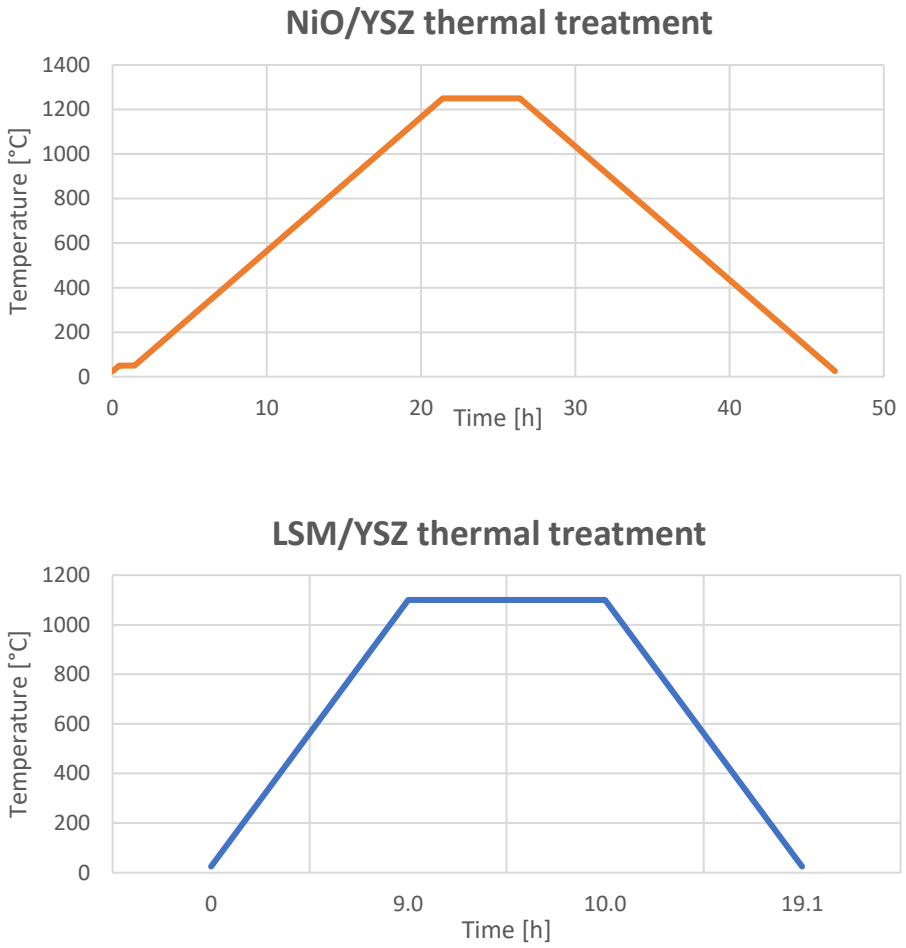

Figure 33| NiO/YSZ and LSM/YSZ thermal treatments

2.7 Electrochemical characterization of cell performance - Electrochemical impedance spectroscopy (EIS)

Electrochemical Impedance Spectroscopy (EIS) is a powerful characterisation technique for investigating electrochemical devices such as batteries, fuel cells, supercapacitors and membranes. EIS consists of the study electrical response of the device while varying the excitation frequency. As every frequency analysis, the component behaviour is characterised by the transfer function, the ratio between the out phasor and the inlet phasor. To this regard, to study the frequency response, EIS was performed applying a small Voltage amplitude (ΔV) and reading the corresponding Alternated Current (AC) (ΔI). The ratio between the voltage amplitude and the current amplitude constitutes the transfer function, which for definition define an impedance ($\bar{Z}$), a physical quantity representing the opposition force of a circuit to the passage of a time-dependent current.

$$\bar{Z} = \frac{\Delta V}{\Delta I} = \frac{|V|}{|I|} \frac{e^{j\omega t}}{e^{j(\omega t+\phi)}} = |Z|\, e^{j\phi}$$

Where ω is the angular frequency, the time and ϕ the angular phase displacement.

In this work, EIS was carried out for measuring 21.7 cm^2 of large cell area (see figure 36) in symmetrical configuration by using the potentiostat *PARSTAT 2273* controlled with the *Powersuite* software.

To measure in symmetrical configuration, the large area cell, the LSM cathode was painted over the active surface of the cell. Then, the cell was heat treated and an additional layer of gold paste was applied as a current collector. As the cell was cracked, the gold paste and the LSM cathode were brushed away from the cracks to avoid a possible short circuit. Once both electrodes were finished, the cell was prepared for measurement by placing it in the holder containing a gold mesh connected with the electrical connections insulated with a high temperature resistant cladding and some stripes of alumina felt on both sides. While the gold mesh was adopted to increase the current collection, the alumina felt was used to give a good cell-gold mesh adhesion, since the cell was slightly bent after sintering. Subsequently the cell is installed in the clamp holder which is placed in the furnace where the door is insulated with a glass fibre blanket to limit thermal losses. The cell holder consists of two plates, each of which is connected to 2 tubes, 1 for the gas inlet and 1 for the gas outlet. The plates have a gas flow pattern to ensure good gas distribution over the active surface of the cell. Following that, the potentiostat was electrically connected to the cell with 4 wires with negligible resistance to detect low current, high current, low voltage and high voltage signals. These signals can be represented as frequency response in Bode (Module vs Frequency and phase vs Frequency) or Nyquist (real vs imaginary) plots, describing the device performances over a wide frequency range (several order of magnitude). An example of Nyquist plot is shown in figure 34.

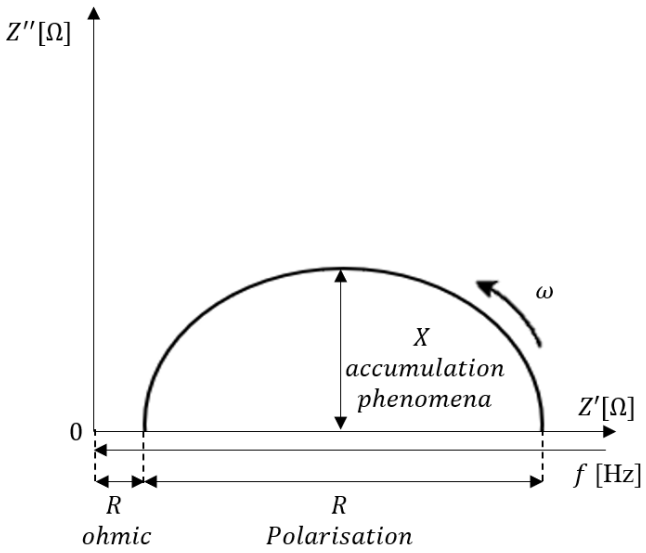

Figure 34| Nyquist plot of an RC element represented in the real (Z') and imaginary (Z'') plane.

As the figure 34 shows, the value from the origin to the lowest frequency intercept of the curve will be from now on called the serial resistance (R ohmic of electrolyte) while the amplitude of the arc the polarisation resistance (R polarisation of electrodes). The sum of polarisation resistance and ohmic resistance define the total resistance. Regarding the distance from the real axis to the curve, this represents the energy accumulation phenomena characterized, in this case, by a capacitor.

Regarding the distance from the real axis to the curve, this represents the energy accumulation phenomena characterized, in this case, by a capacitor.

Next, the oven is heated up to 950°C at a heating rate of 5°C/min, the measurements of the cell were conducted in air every 50°C from the temperature of 950°C downwards to of 650°C. A frequency range of $1{,}00 \cdot 10^3$kHz to 100 mHz and amplitude of 50 mV were set. Then the measurements were fitted through the program *Zview* to define an equivalent circuit, an arrangement of electrical component characteristics and arrangement of which have the same frequency response as the device. The components of an equivalent circuit can have a correspondence of the various characteristics of the real system (i.e., mass transport, activation). The electrical elements are passive components: Resistance (R), capacitor (C) and inductor (L) representing active and reactive power losses but can be also distributed elements which represent electrochemical or mass and ionic transport phenomena such as the Constant Phase Element (CPE) which describes a distributed charge accumulation on rough irregular electrode surface [64].

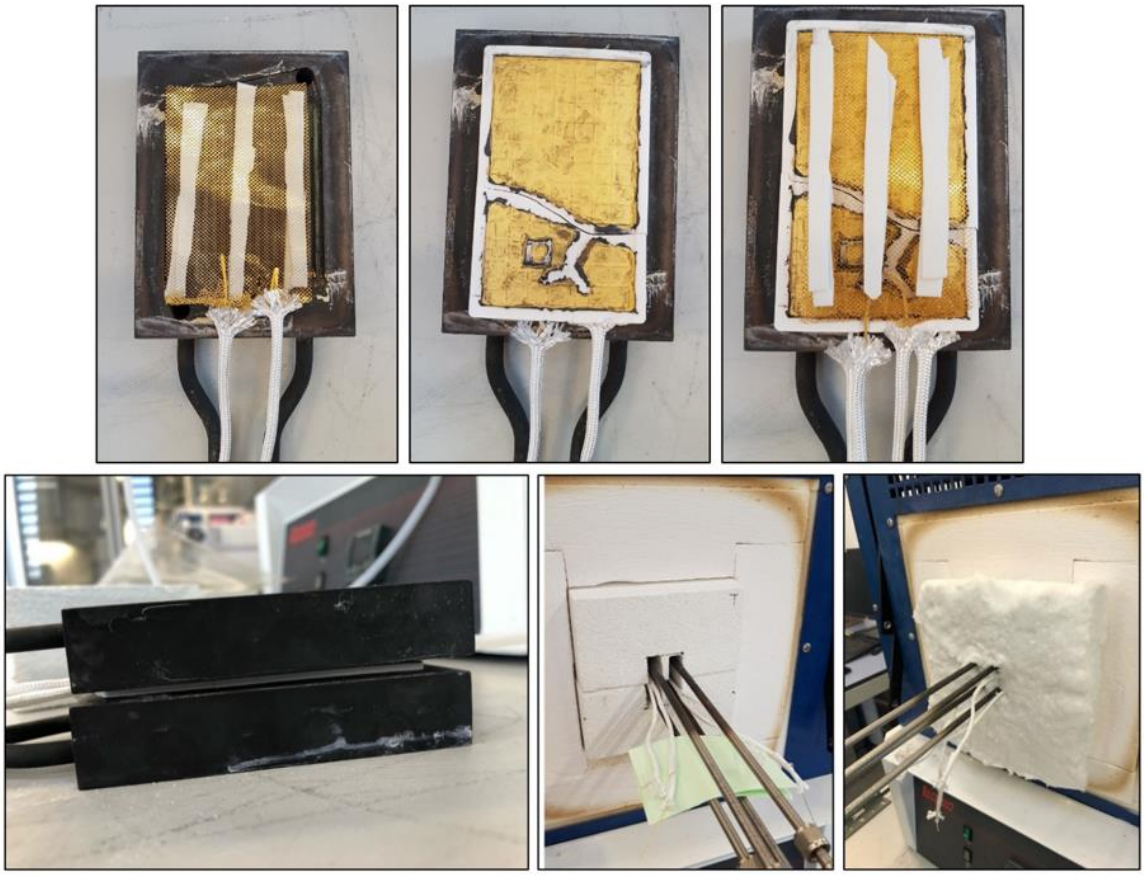

Figure 35| Example of set-up sequence for EIS of large area cell in symmetrical configuration. The figure shows the gold mesh and alumina felt placing in the holder followed by the cell allocation and another layer of mesh and alumina felt. The holder is subsequently placed in the furnace.

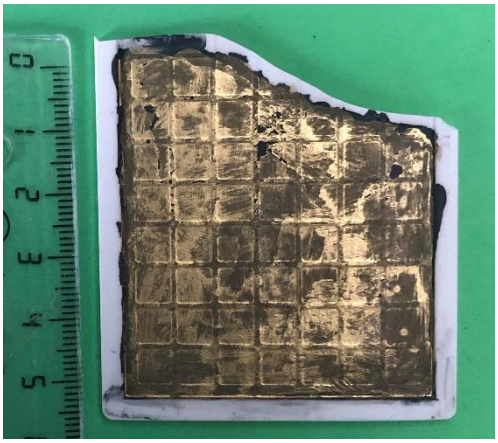

Figure 36| Large cell area used for EIS measurement- The piece has an active area of 21.7 cm^2

2.8 Microstructural characterization - Scanning Electron Microscopy (SEM)

A Scanning Electron Microscope Zeiss Auriga with Schottky emitter, 30kV FESEM column equipped with an Oxford Instruments EDS Xray detector was used to characterize the samples. The main parameters were an acceleration tension of 20 kV, aperture size of 30 μm and working distance between 5-8 mm. The SEM instrument consist of four main systems: an electron emitter, electron optics column, a vacuum system, and signal detection & display. The electron beam is focused on the sample surface as it passes through a set of magnetic lenses to control and modify the beam. When the beam reaches the sample surface, as a result of electron-sample interactions, various signals are captured from the detectors and electronically translated in an image. The main signals the SEM can measure are Backscattered Electrons (BSE), Secondary Electrons (SE) and X-rays. The BSE signal is the elastic reflection of the electrons and provides information on topography, sample composition and crystallography.

Figure 37| SEM Zeiss Auriga with Schottkey emitter, 30kV FESEM column and Oxfor Instruments EDS Xray detector at IREC facilities.

The SEs signal is typically used to provide information about the topography of the sample's surface, since the detected signal is due to the emission of electrons of the sample after the beam-sample interaction. X-ray are emitted by each type of atoms as a result of the sample's atoms excitation by the beam and it is used to identify the chemical elements and their amount.

2.9 Sample preparation for SEM analysis

Preliminary step to perform a microstructural characterisation through the SEM, the sample requires embedding, polishing and metal sputtering. First, the cross section of interest was placed in an iron clip. After the sample and iron clip placed in the centre of a mould, epoxy resin and thermoset were mixed in weight proportion of 25 to 3 avoiding any air bubbles. The mixture was poured in the mould, covering completely the sample, and left to dry overnight. After the resin hardened, the embedded sample was polished in the *TECNIMETAL* machine under water flow with different abrasive papers of different grits. In our case we used 320, 500, 800, 1200, 2400 and 4000 grit, from the courser to the finer. During the paper swapping, the sample was washed under water and dried with compressed air to remove the resin scratched residues, and to evaluate surface quality by eye. After the wet polishing, the polishing plate was replaced with diamond paste plates, first 3 μm particle size followed by 1 μm particle size.

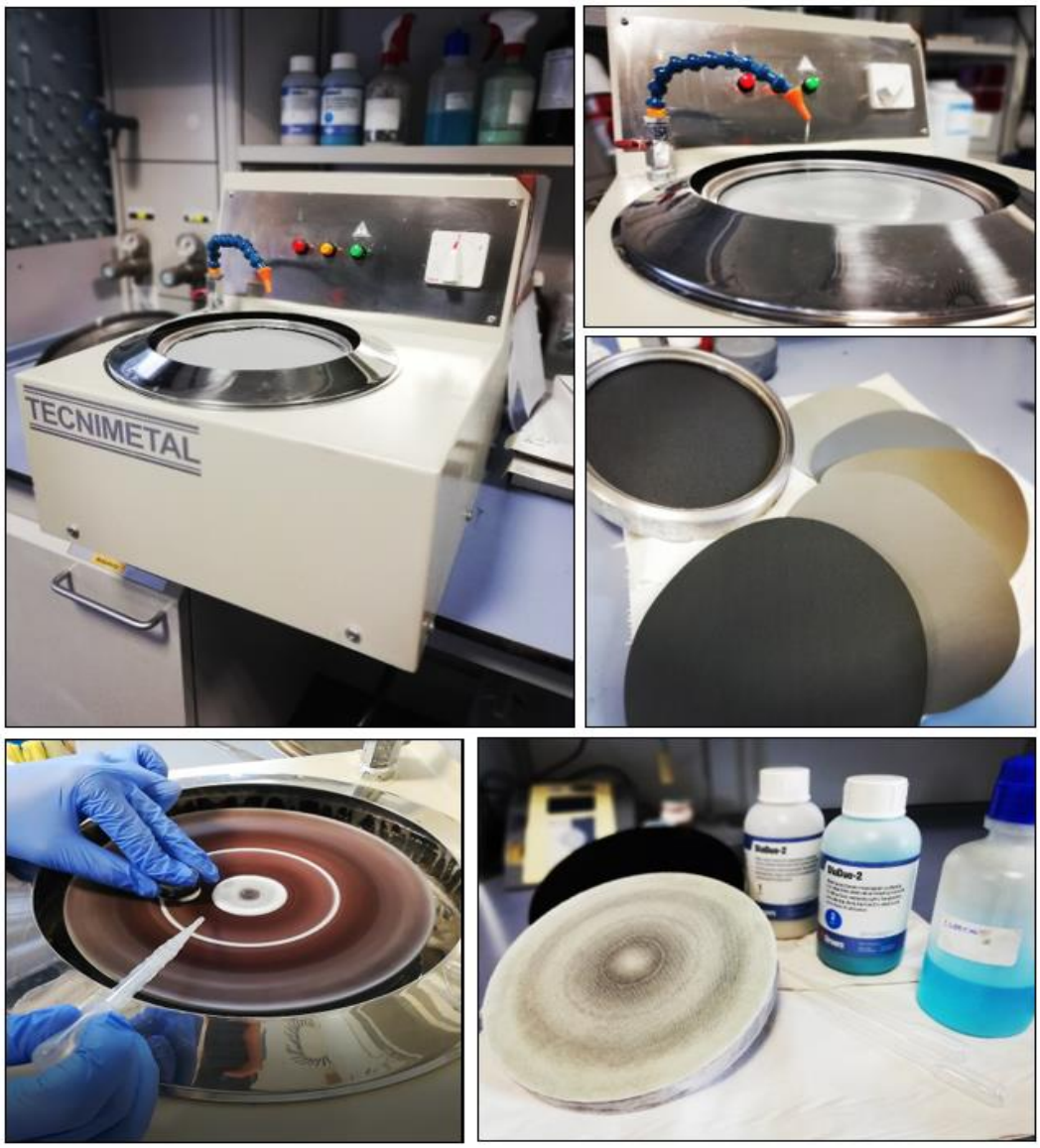

Figure 38| Tecnimetal polishing machine and equipment. The figure shows the polishing machine with the equipped water nozzles, the paper with different grits and the diamond paste plates with the diamond paste containers and lubricant.

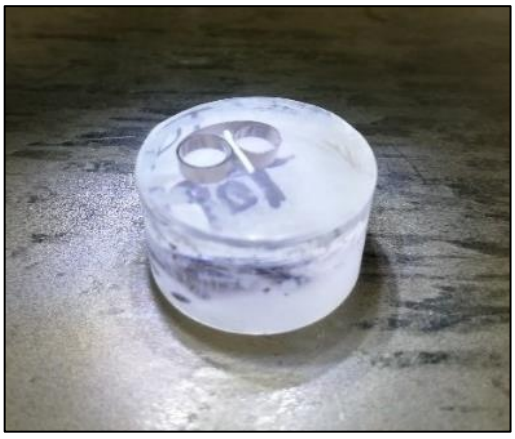

Figure 39| Embedded sample into resin after polishing.

Following the polishing step, a carbon tape path was applied from the top of the embedded sample to the SEM sample holder beneath to create a percolated path. The sample is then placed in the sputtering chamber. Deposition of gold was performed via an argon plasma at a pressure between 2 and 4 10^{-2}mBar with a current of 85 mA for 30 seconds. The top surface was coated this way to make the sample conductive and fulfil charge evacuation requirements for the SEM.

Figure 40| Sputtering machine at IREC facilities. The figures highlight the sputtering process and the sample after gold coating deposition, resulting opaquer and yellow.

Chapter 3 | Fabrication and design

3.1 Design consideration for printing and processing

3.1.1. Large area cell

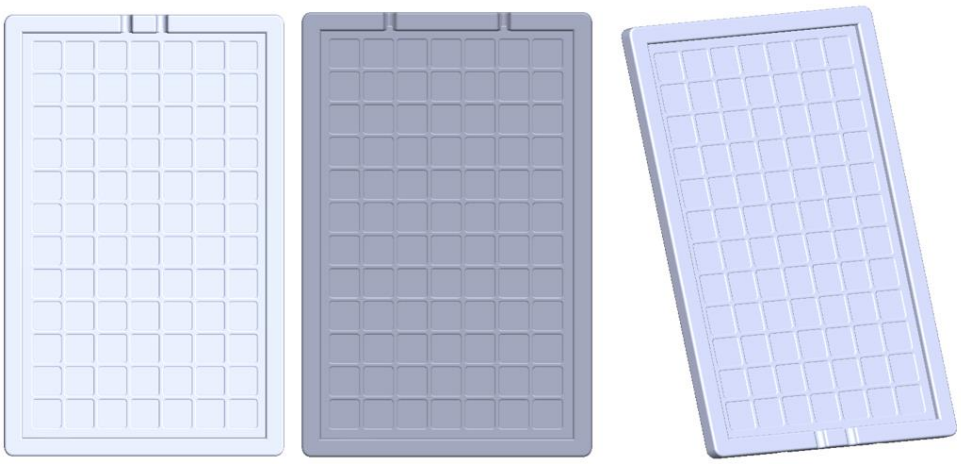

Figure 41| CAD design of Large area cell with squares pattern

One of the group's goal is to print full standard stacks in one single production step. To this aim the first step was to prove the ability to 3D print standard size self-standing electrolytes. The design of this cell was based on a 60x95 mm^2 (WxL) area. The CAD model of this cell was designed with a 4 mm wide and 3,55 thick rectangular frame to support the membrane and to be used later as a sealing surface on the electrical test station. In addition, the frame has two grooves on each side to allow for electrical connections, the position of the connection ports is shifted from one side to the other to avoid a possible short circuit. The membrane was designed to be 0,625 mm total thickness. To facilitate hand manipulation and increase success chances structural nerves at 5 mm distance were added and chamfered at 45°C with a radius of 0,5 mm to avoid stress areas. Each nerve is 0,105 mm thick and 1 mm wide.

Despite the electrodes thickness is affected by the type of deposition process, the electrolyte deals with a trade-off between structural stability and nerves thickness. The greater the thickness of the nerves, the greater the thickness of the electrolyte, which increase the cell stiffness but also the ASR of the cell. It is therefore clear that the choice of a finer or coarser square pattern and the thickness of the nerves are the main parameters that lead to an increase or decrease in performance compared to a simple flat cell. This large area electrolyte with square pattern was fabricated by using of the *Ceramaker* with a printing time about 1 day.

3.1.2. Spiral cells design

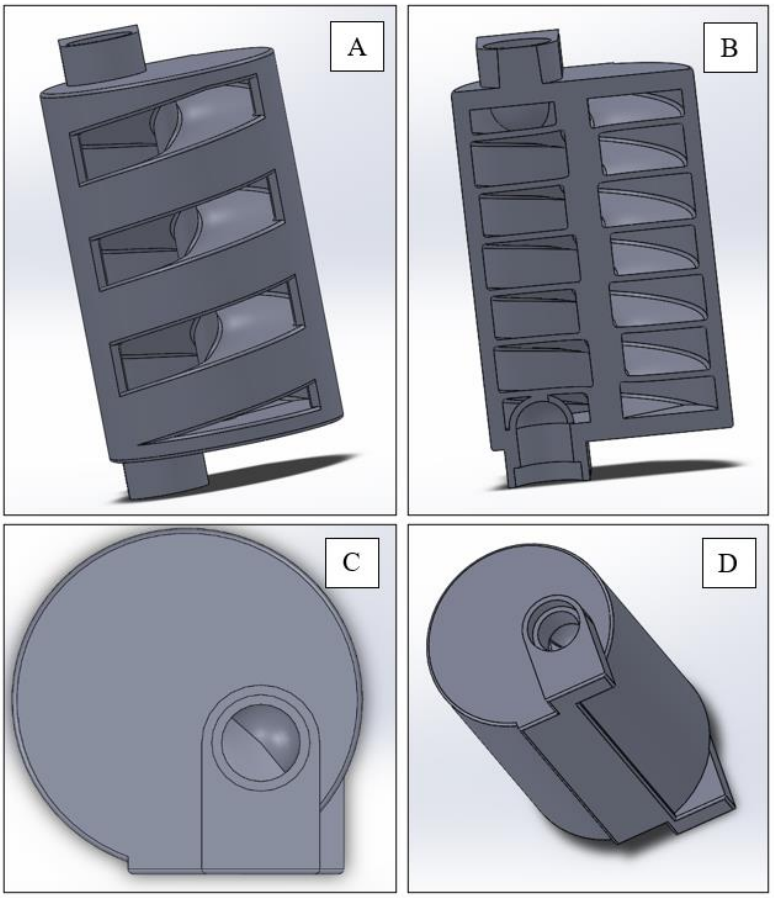

Figure 42| CAD design of the electrolyte supported cell with spiral geometry.

On a different concept, this model was designed to produce small volume fuel cell for intermediate power requirement applications such as personal electric mobility devices. Pursued geometrical design specifications were high inlet fuel percentage consumption and low volume to active surface ratio. To this end a spiral-like electrolyte design was proposed (see fig 42-A). Maximum power, fuel consumption efficiency and active surface to volume ratio can be tuned by parameters such as helix pitch, cell length and diameter. Moreover, this design provides a steady support that will facilitate the production and manipulation of a cell with low self-supporting electrolyte thickness.

As this complex design was in early stage of development, the geometries were simplified to facilitate post processing (e.g., cleaning and thermal treatment). To this regard, the spiral geometry membrane was 0.45 mm thick and supported through a 17.8 mm diameter tubular shell. The inner side of the 253 mm long spiral path is the fuel channel, and the outer side is the airflow path, defining an open cathode cell. The helix pitch was 8 mm, and the membrane surface was 1466 mm^2. The open cathode was adopted to aid the binder removal process avoiding cracks formation and to help the removing of uncured paste. Furthermore, this configuration allows the cell to work in atmosphere with air.

Moreover, as shown in the vertical cross section (figure 39B), the inlet and outlet of the spiral anode path were constituted of manifolds with elbow bend connection to allow a smooth gas path, avoiding fluid dynamic losses and to allow an easier cleaning, strengthening the beginning of the path and preventing membrane breaking. In figure 42-C and 42-D is shown in different

views the implementation of a flat platform in design. The platform allows to avoid unwanted movements during the scraping process that could cause misalignment of layers in the construction process.

As the large area cell, the spiral cells were printed in 3YSZ by means of the *Ceramaker* printer. The printing process was about 3 days long.

3.2 Processing after printing

3.2.1 Cleaning of the 3D printed parts

Simple and easy access designs such as large area cells were cleaned by delicately brushing the piece with the *Ceracleaner* (cleaning solution made by *3D Ceram*). Regarding the spiral design, the internal chamber it was cleaned first without removing the uncured paste from the cathode side to help support the thin and fragile membrane. By using 0.25 mm^2 wire, *3D Ceram* cleaning solution, pipettes, a gentle jet of compressed air and several ultrasonic baths, uncured paste was completely removed from the fuel chamber. Afterwards the uncured paste was removed from the outside with a brush soaked in a cleaning solution and ultrasonic baths. As a result of the cleaning, 2 spirals and large cell area were successfully cleaned obtaining the so-called green piece (solid part before thermal treatment).

To regard the plastic spiral and the fluidity tool, as they were printed with free solid load resin, the cleaning process was carried out by removing the additional support through a spatula and the impregnated uncured resin through *Isopropanol (IPA)* bath.

The time for cleaning the 3D printed part made in 3YSZ was about 20 h for the spiral cell and a couple of hours for the large cell area. The plastic spirals were cleaned in isopropyl alcohol for half hour.

Figure 43| Equipment for parts cleaning. In the figure are shown the Ceracleaner solution, the brush, the shaped wire, the compressed air nozzle and the protective mask and glasses.

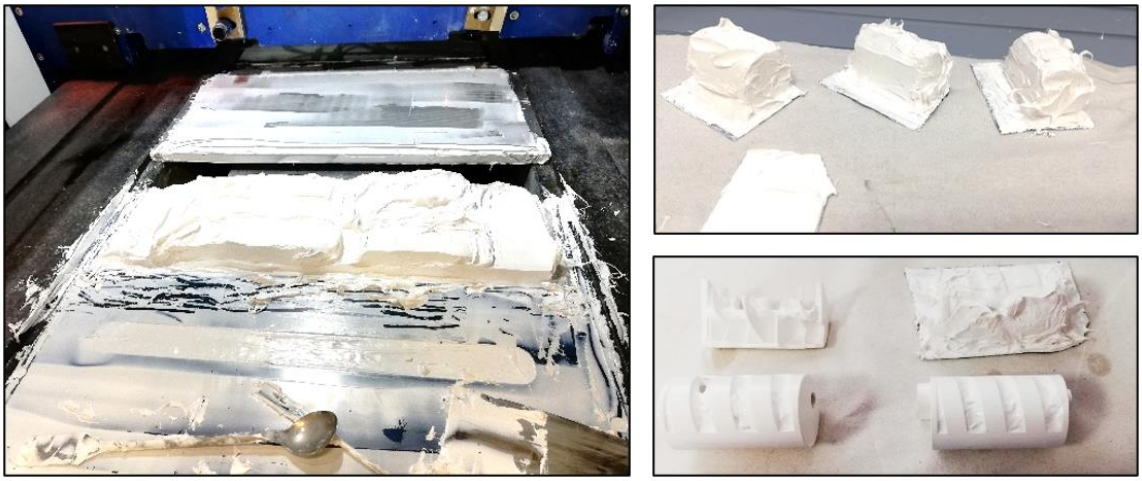

Figure 44| Uncovering of parts. It is worth notice as one piece undergoes blade collision which caused layer misalignment and piece destroying.

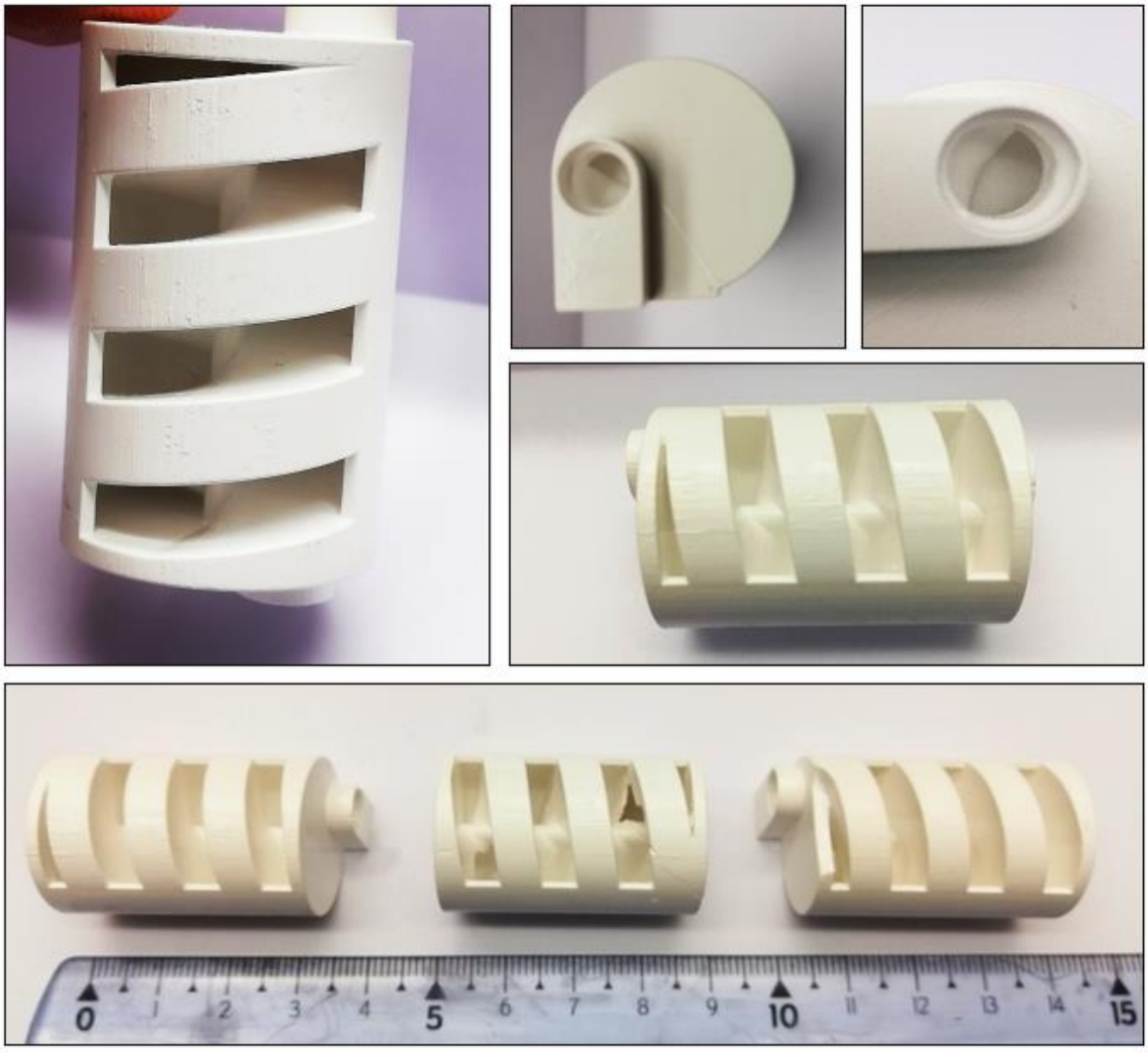

Figure 45| Tubular cells with spiral design after the cleaning process (green). Three green pieces were successfully printed and two of these perfectly cleaned without breaking the membrane.

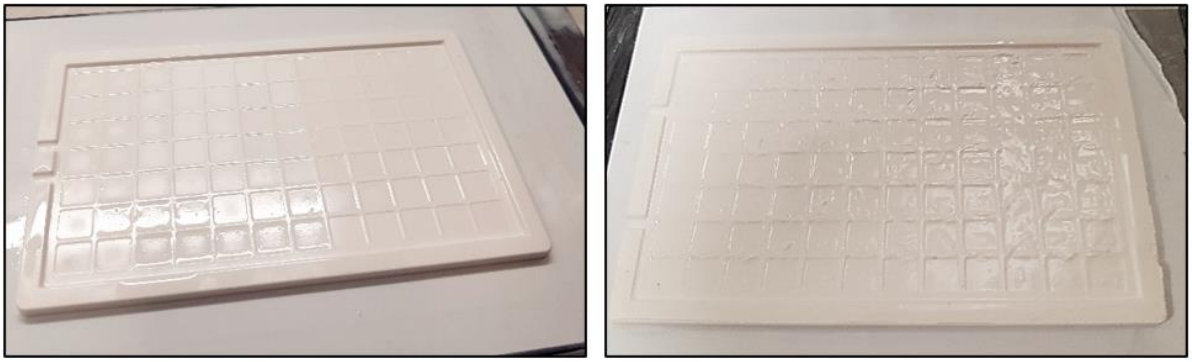

Figure 46| Green of large flat electrolyte with square pattern printed at IREC facilities. In the figure it is possible notice how the movement of the blade partially destroyed the square pattern on one side during the recoating process.

3.2.2 Thermal treatments

3.2.2.1 Debinding and sintering process of 3YSZ electrolyte

Following the cleaning step, the green pieces were ready to be heat treated. As shown in the graph 44, the debinding and sintering process can be subdivided in three regions: binders' removal, gas swapping and sintering.

The binders' removal process consists in a very slow (about 3 days) heating of the part into a furnace under nitrogen gas flow, to prevent high evaporation rate which may lead to cracks and severe distortion of the piece. Once the majority of binders' evaporation and removal is finished, at constant temperature pallier and constant gas flow rate of 500 ml/min, the inert gas is gradually replaced by the air, burning the residual binders. Following the gas swapping stage, the sintering process starts by increasing the furnace temperature above 1000 °C until gradually reaching the 3YSZ sintering temperature of 1450 °C. The sintering process is carried out below the component melting temperature where shrinkage and porosity reduction lead to particle coalescence, reducing the particles surface and leading to a more stable configuration. During the first shrinkage stage, necks formation takes place along the contact region between close particles, forming grain boundaries while every interstitial space between the different particles become a pore. Continuing to perform the sintering, these pores become smaller and smaller with spherical dimension. Once the sintering process is complete reaching the desired density, the component is cooled down at a rate of 3 °C/min.

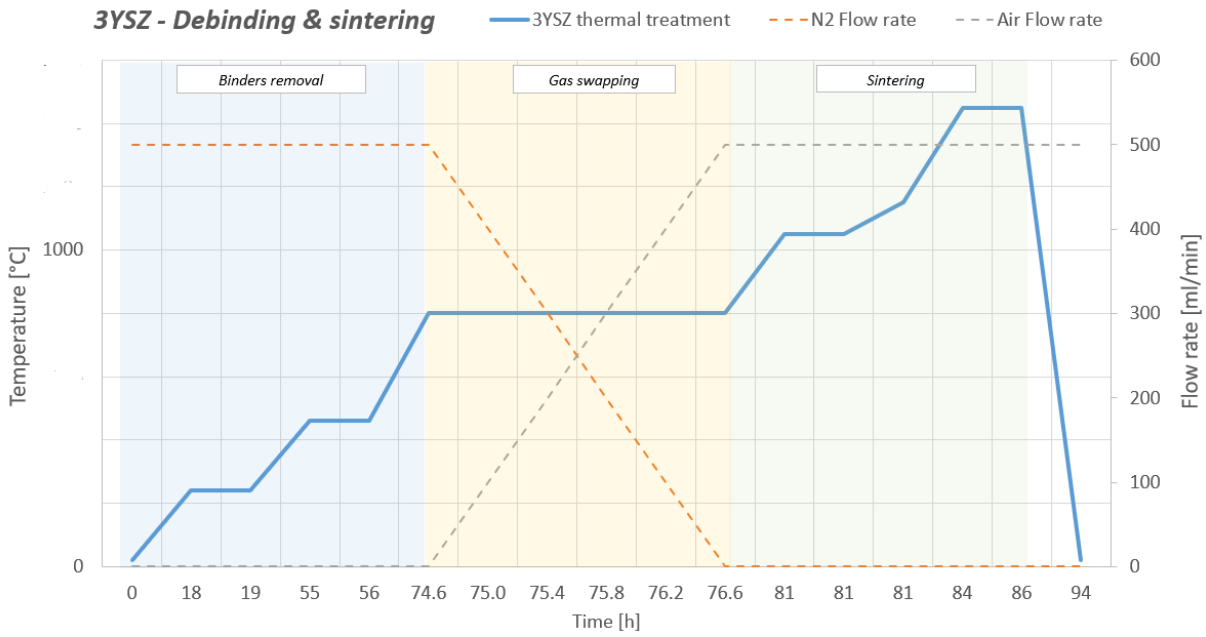

Figure 47| 3YSZ thermal treatment. The figure shows the 3YSZ debinding and sintering process with a reference temperature of 1000°C for copyright reasons. The different stages of the process are highlighted, binders removal (blue), gas swapping (yellow) and sintering (green).

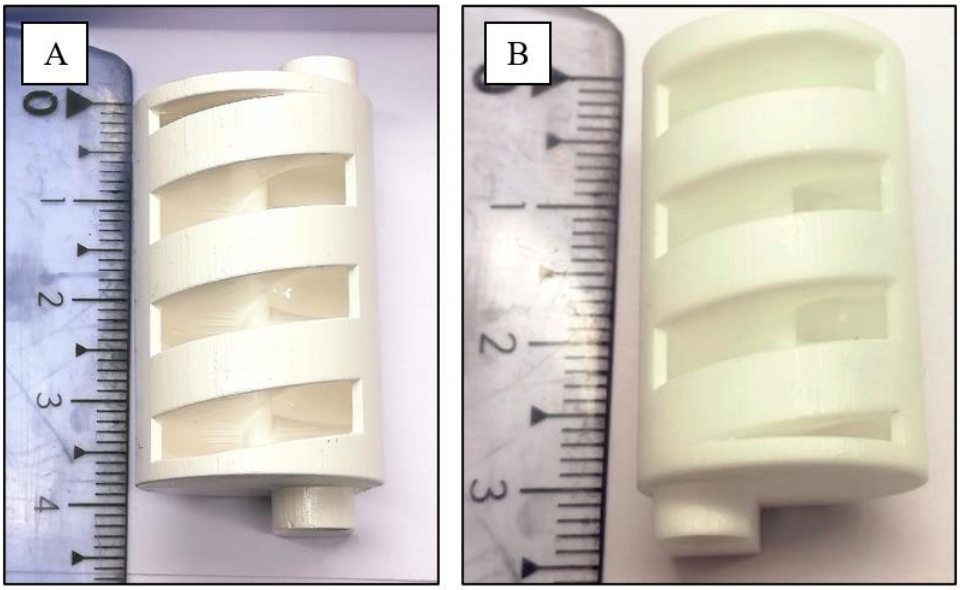

Figure 48| Tubular cell with spiral design before (figure A) and after the sintering process (figure B). In the figure can be noticed as the piece has shrunk after the sintering, achieving the desired dimension set in the CAD model.

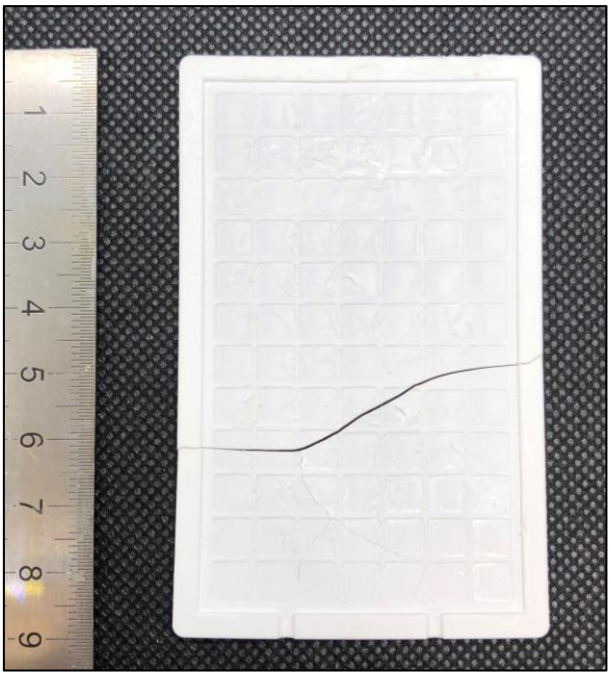

Figure 49| Large area cell after the thermal treatment. As the figure shows, the cell was cracked due to distortions caused by the thermal treatment, in which, even if is a very low and delicate process, the big dimension of the cell and the thermal stresses generated affect the mechanical stability according to the Griffith theory.

Chapter 4 | Formulation of the ink and functionalization

4.1 Rheology evaluation of anode inks

Three NiO-YSZ inks were formulated, and their rheological properties were characterized. The formulation of the inks I1, I2, I3 is reported in Chapter 2. Viscosity and inks-substrate interaction are the main parameters to characterise the inks for injection. Using the rotational viscometer, the viscosity of the anode slurries was measured in the shear rate range 10-1600 s-1.

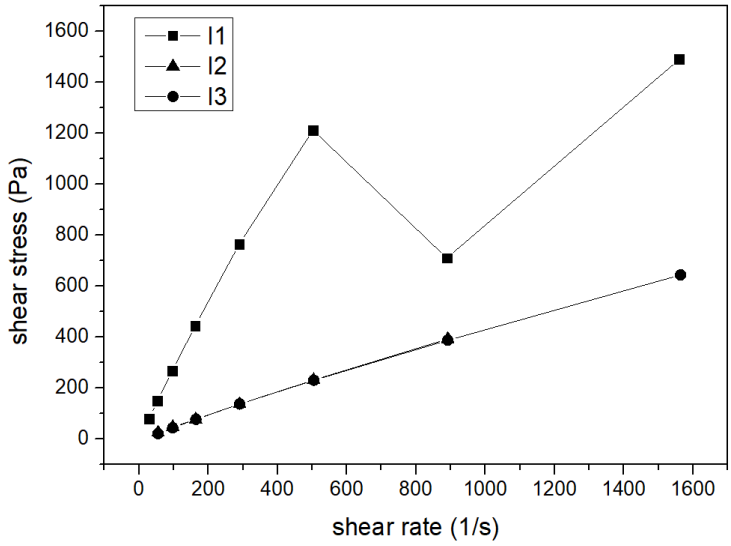

Figure 50 | Shear stress curve of anode inks 1, 2, 3.

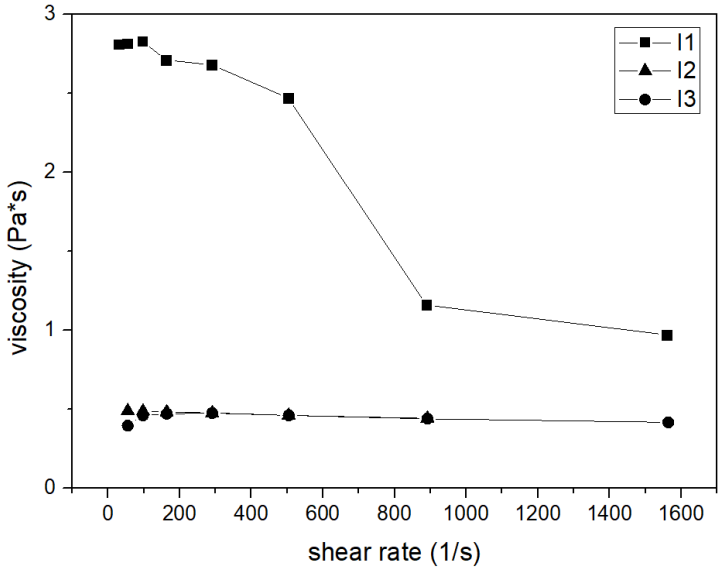

Figure 51 | Viscosity curve of anode inks 1, 2, 3. The inks 2, 3 showed a viscosity suitable for the injection inside the spiral.

Considering figure 50 and figure 51, ink 1 is the one showing the higher viscosity (around 2.5-3 Pa s for shear rates between 10-600 s^{-1}). This formulation was prepared using PVP K90 as a binder. In the newer formulations (ink 2 and 3) the K90 binder was removed and the viscosity was reduced to ≈0.5 Pa s with respect to the same shear rate range.

As shown in figure 51, the viscosity of ink1 decreases and shear stress increases as the shear rate is increasing showing a shear thinning behaviour. Inks 2, 3 presented an almost constant viscosity during all the measurement and shear stress values proportional to the shear rate. Therefore, it can be concluded that these inks presented a Newtonian-type behaviour.

As the goal was to inject the ink with lower viscosity and lower surface tension on the 3 YSZ spiral channel, ink 2 and 3 were tested through a fluidity measurement tool, described in the experimental section. As shown in figure 52, both inks arrived at the end of the 6.4 cm long path. However, ink 3' reached hundredths of a second earlier the end of the YSZ tile, demonstrating to be the best choice for the injection inside the printed spiral.

Figure 52 | Fluidity test sequence along the 6.4 cm long path with a sliding time about 3 seconds.

4.2 Deposition and drying of anode inks

Some printability tests were made on substrates of 3YSZ. The fresh inks were deposited by hand with a syringe on flat substrates and left to dry on a hot plate at 50°C for 1 hour. After the drying process the samples were sintered at 1250 °C as described in chapter 3. As shown in figure 53, the layer deposited with ink 1 showed only cracks after the drying process. The layer deposited with ink 2 showed a good homogeneity and it did not present any cracks after sintering. The sample obtained with ink 3 showed some small cracks after drying. The deposition of the layers was carried out by hand the in some cases the cracks where due to the large thickness of the layer.

Overall, the layers obtained from the inks showed a good distribution. The few cracks observed were attributed to the deposition process carried out by hand. In particular, the samples deposited using ink 2 and ink 3 showed the best morphological distribution.

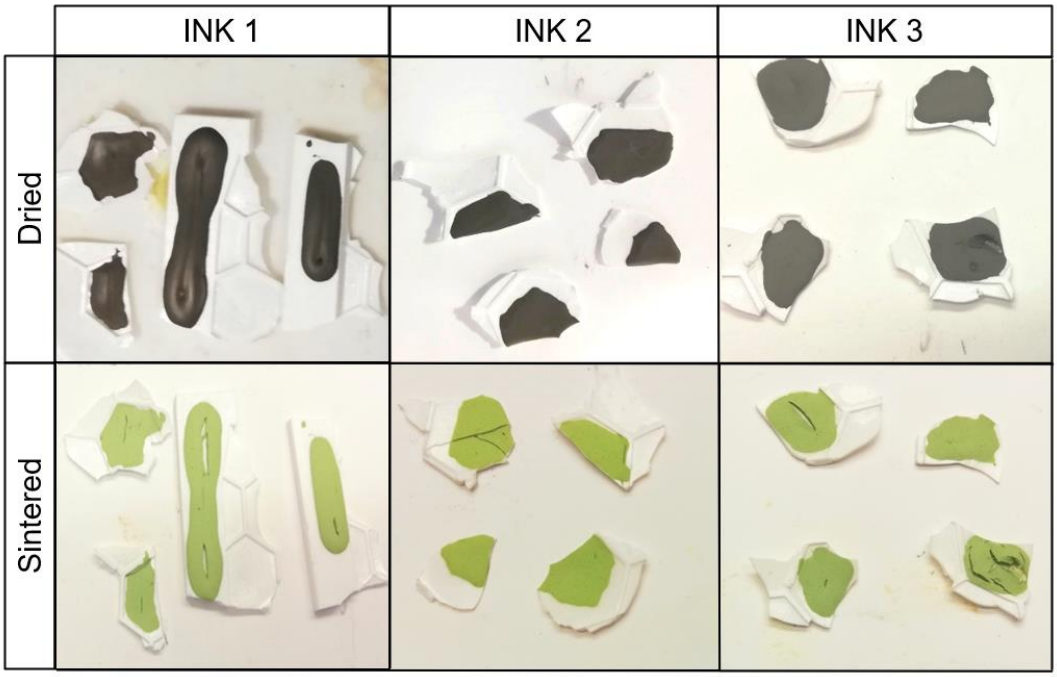

Figure 53| Dried and sintered anode inks samples. The sintered ink sample 2 in the top left-hand corner was broken during the handling of the component. Similarly, the dried and then sintered sample 3 in the bottom right shows cracks caused during its handling.

4.3 SEM characterisation

SEM analysis were performed to evaluate the topography of the deposited and sintered NiO/YSZ inks with the 28% vol of solid loading onto 3YSZ substrate. Since the SEM evaluation aimed a microstructural characterisation, the sample were analysed through secondary electrons signal.

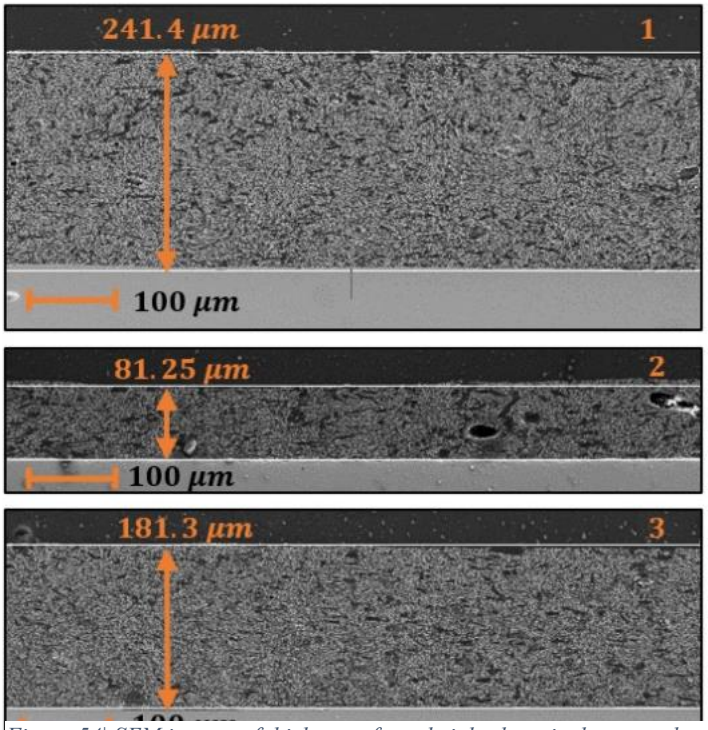

Figure 54| SEM images of thickness of anode inks deposited on sample surfaces- Magnification 500X.

First of all, at a magnification of about 500X, the thickness of the deposited anode inks is assessed by the SEM images. As shown in figure 54, mechanical deposition by injection of a syringe exhibits various thicknesses, for example, while I1 is ≈241.4 µm thick, I2 and I3 are ≈81.25 µm, ≈181.3 µm, respectively.

Comparing the inks, ink 2 shows some holes of 25 µm, which could be attributed to poor organic dispersion during the mixing process, while ink 1 and ink 3 showed an excellent distribution.

However, to have a more exhaustive microstructural point of view, a more accurate analysis at higher magnification is shown in figure 54, where the pictures on the

left side have been captured with a magnification of 5 KX. At this scale, it is possible observe the lamellar and spherical holes obtained from the two pore formers used: graphite and PMMA. In addition, the deposited layers showed a good open porosity, similar in all the three cases. This it is highlighted in the right column of pictures, representative of a magnification of 10KX.

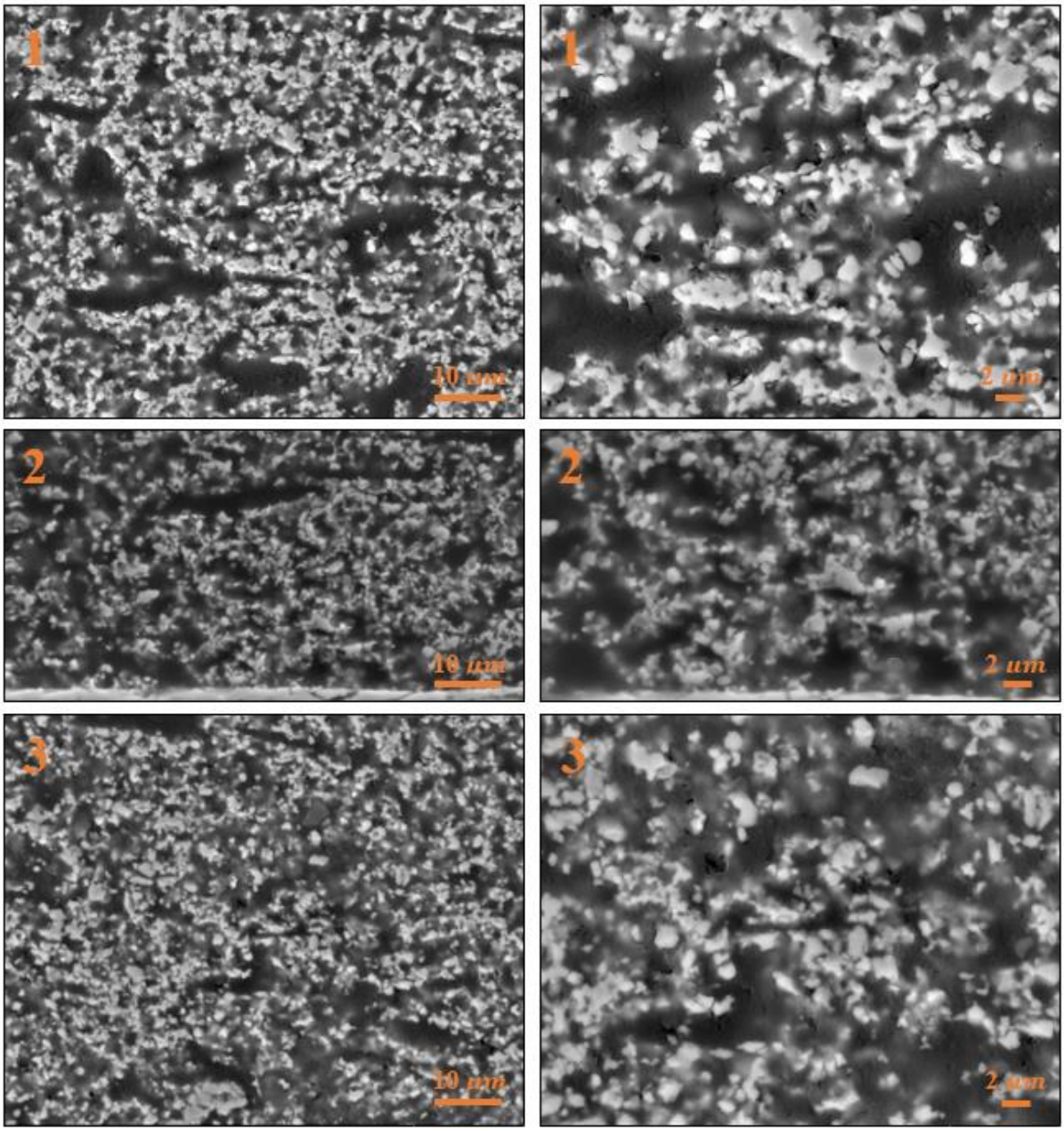

Figure 55| SEM images of anode ink at magnification of 5KX (left side) and 10 KX (right side).

Figure 56 shown a summary of the results of the characterization of the three produced inks. I2 and I3, which were prepared removing the PVP-K90 binder presented good rheological properties, feasible with the application. The microstructure of the layers deposited starting from the inks I1, I2 and I3 were characterised by high interconnected porosity.

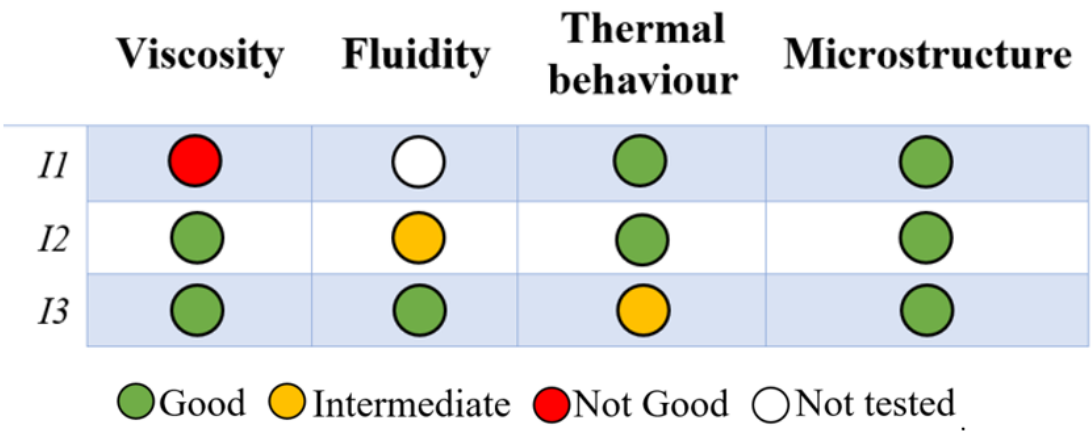

Figure 56| Trade off table of functional anode inks

4.4 Deposition process of the anode inside the spiral

Once the anode ink formulation was defined based on the rheological and microstructural properties, the injection test was carried out in the spiral manufactured by means of *Formlabs* printer, following the procedure described in chapter 2. The plastic spiral tested has the same geometries as the real ceramic cell, such as pitch and diameter, but as shown in figure 57, it has 3 reversals instead of 4, which affect the height of the sample. The injected plastic cell shows good wetting surfaces along the entire spiral path. The coverage of the ink surfaces within the fuel electrode path is highlighted in the cross section of the plastic spiral. The image, representing the part cut with a saw, shows the cross section view of the plastic spiral. The ink was injected from both sides to ensure the complete cover of the channel. An accumulation of ink was highlighted at the inlet of the spiral. This problem could be easily avoided increasing the deposition time to improve the distribution of the ink inside the internal chamber and avowing a possible clogging of the channel. Overall, the injection of the fuel electrode ink was successfully carried out demonstrating the that the rheological properties of the slurry are suitable for this application.

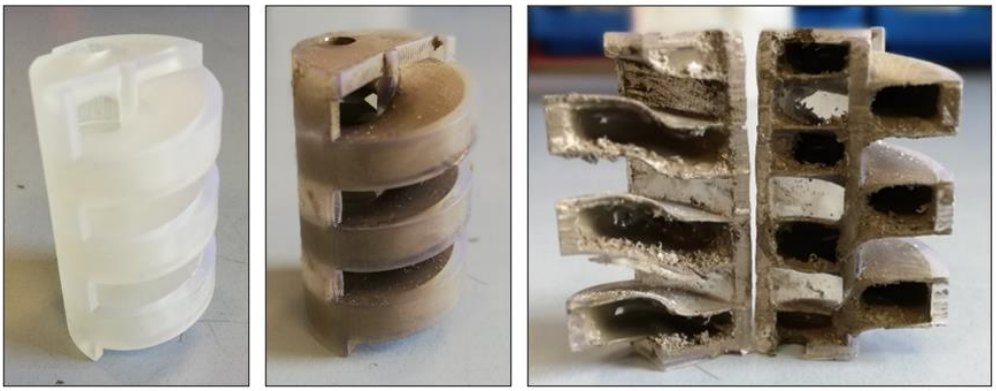

Figure 57| Ink 3' injection sequence in the plastic spiral and cross section after the test.

Figure 58| Injected closed cathode ceramic dummy cell

An additional test was carried out in a dummy ceramic spiral. The sample was printed with 8YSZ and presented a slightly different design. In this case both fuel and oxygen electrode sides were closed. The spiral cracked already after sintering and therefore was used as additional fluidity test. The injection procedure in the ceramic cell was carried out in the same way as the injection into the plastic cell. In this case both fuel and oxygen electrode channels were injected, each one form one side, in order to evaluate the penetration of the ink inside the two channels. As shown in the figure 58, one side presented an excessive accumulation of ink. This was probably due to the irregular surface caused by the cracks present all around the spiral. However, the ink was successfully deposited on the second channel (the top part of the spiral in figure 58). In this side the ink covered more than half of the path, which is the fundamental requirement to be sure to have a homogenous deposition when the channel is injected from both sides. The fuel electrode showed delamination in some points, this was due to the thickness of the layer in some points. This problem could be easily solved, as already mentioned, increasing the deposition times in order to allow a more uniform distribution of the ink.

Functionalized parts of the spiral were observed at SEM in cross section after embedding in epoxy resin and polishing with carbide paper and diamond paste. Figure 59 shows some micrographs of two zones of the spiral, the top and the middle of the membrane.

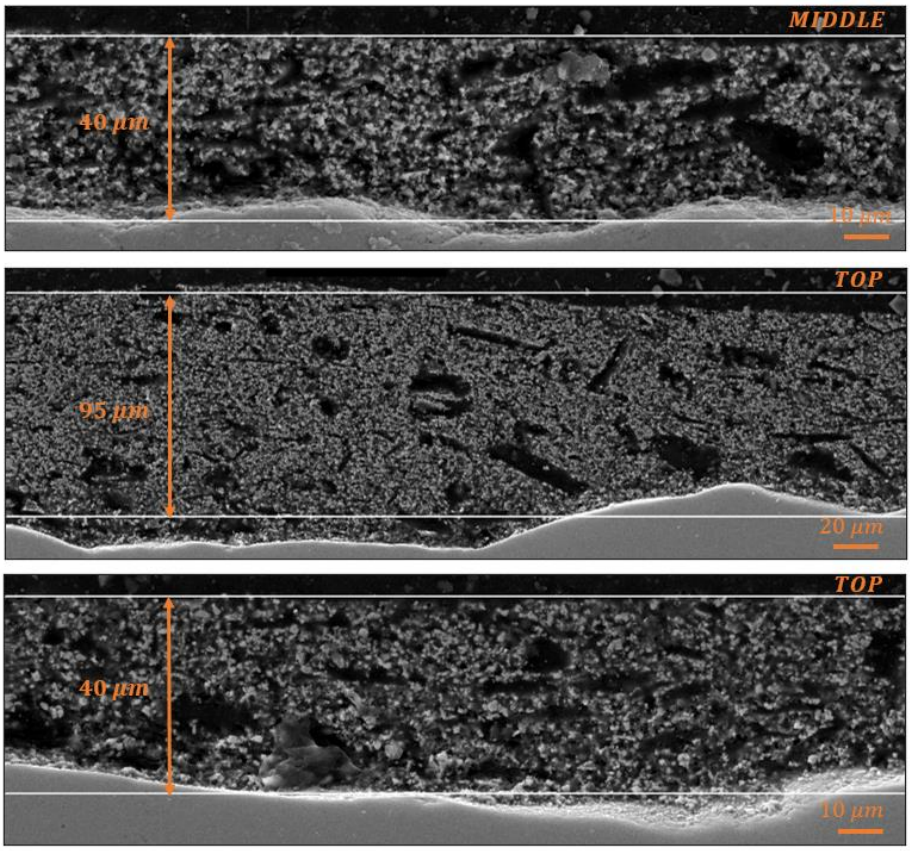

Figure 59| SEM images of the thicknesses of the anodic layers on the ceramic membrane at the top and in the middle of the spiral path.

As shown in figure 59, the thickness in the top side presented a good distribution with thickness compatible for the utilization of the deposited layers as electrodes for application in SOCs. The different thicknesses measured (about 40 µm and 95 µm) where caused by the morphology of the membrane. The central part of the spiral presented a layer with a homogeneous thickness of 40 µm. In all cases the microstructure of the layer showed an excellent open porosity granted by the utilization of PMMA and graphite in the formulation of the inks. The distribution of the inks can be further improved with a more careful control of the deposition process.

In this respect, before heat-treating the component, a support was used to allow excess ink to drain away, reducing the thickness of the anodic layer and preventing clogging of the channel (figure 60).

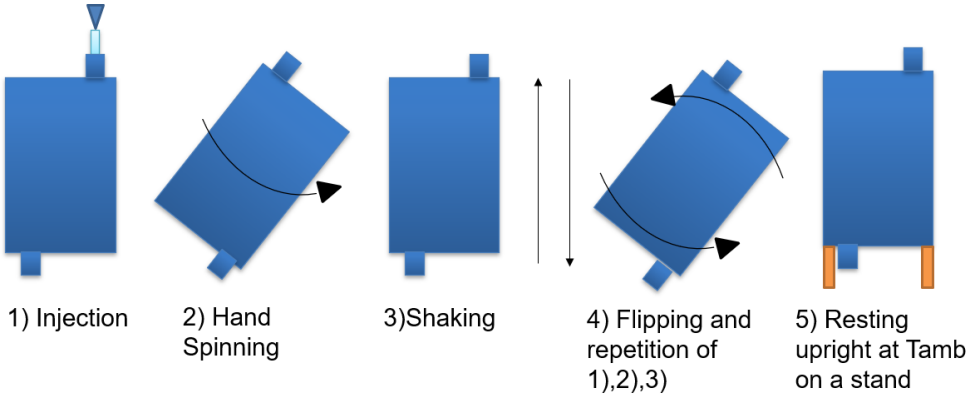

Figure 60| Modified injection procedure with stand implementation to drain the excess of ink

The new spirals printed were functionalized with the fuel electrode ink following this new procedure. Very small cracks were observed in the electrolyte structure after injection, as shown in figure 61. The unknown cracks formation was attributed to the manual and mechanical cleaning process, but further attempts should rule out the debinding and sintering process. In this case the NiO-YSZ no clogging of the ink was observed at the inlet and outlet of the spirals due to the more careful control of the deposition procedure. After sintering of the layers, ethanol was injected in order to exclude possible clogging in the central part of the spirals. Some small cracks of the layer were highlighted at the inlet of the spiral channel, as shown in figure 61.

The optimized procedure allowed a correct distribution of the ink and a successful deposition inside the inner channel of the spirals, as shown in figure 62.

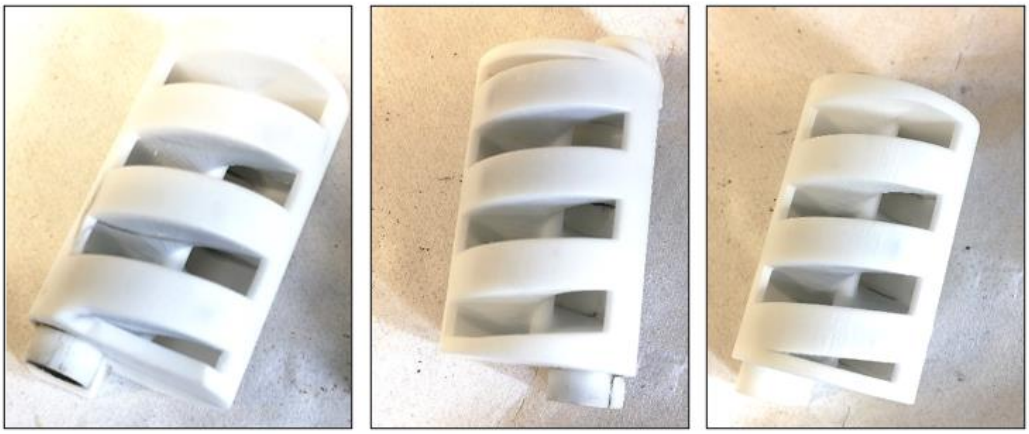

Figure 61| Spirals after anode ink I3 injection. In the figure some cracks highlighted after the injection are shown (black lines)

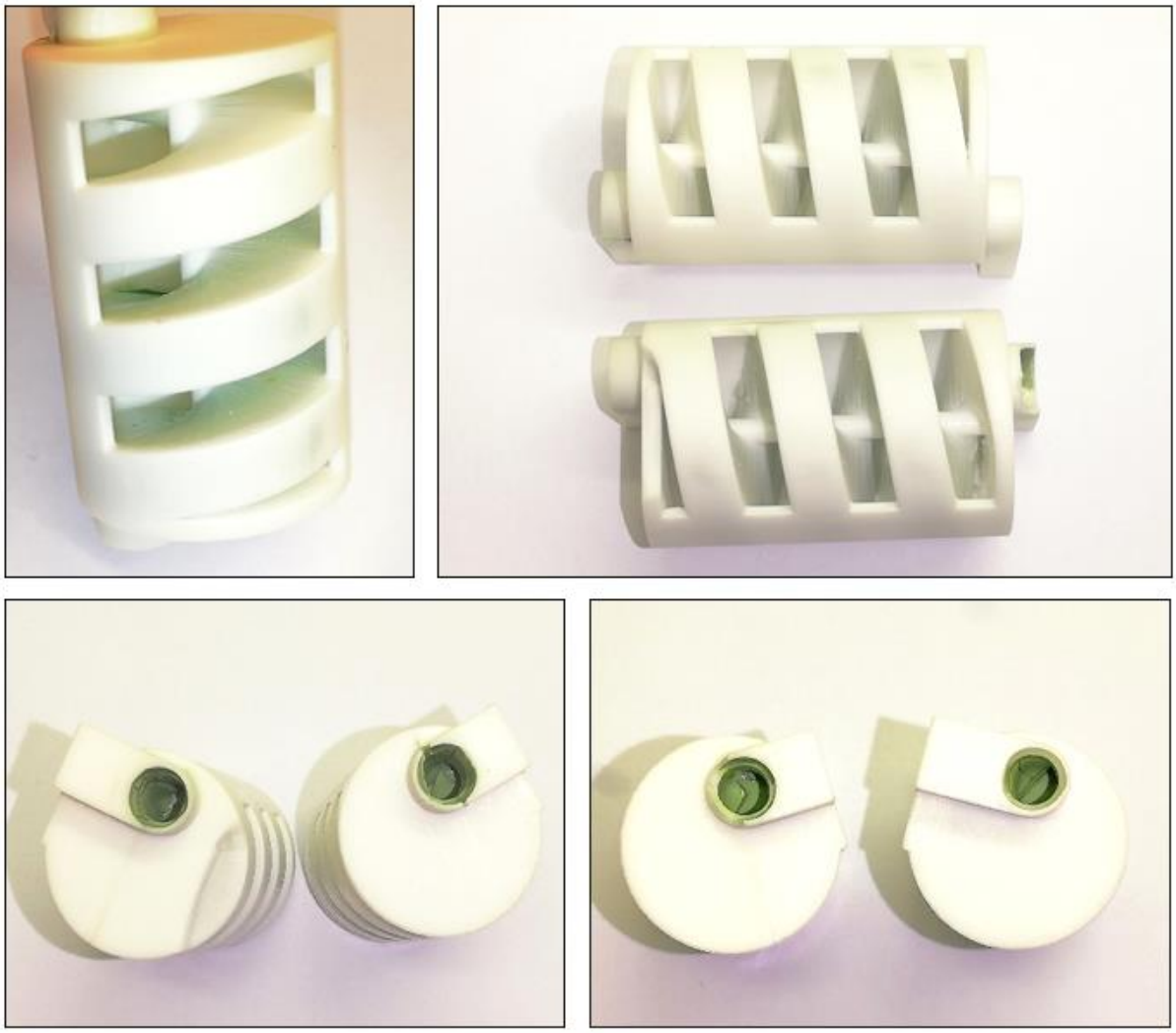

Figure 62| Injected ceramic spiral with open cathode design. The figure shown the spiral injected and sintered with the I3 NiO/YSZ.

Chapter 5 | Electrochemical characterization of the cell

5.1 Impedance spectroscopy measurements of large area cell

The Large cell area was electrochemically tested at IREC facilities and the measurements were obtained from PARSTAT with the set-up described in chapter 2. Figure 63 and figure 64, show the Nyquist plots of the impedance spectra obtained in air at the different temperatures (from 650 °C to 950 °C). The temperature dependence of the impedance spectra can be immediately noticed by observing the Nyquist plots.

The spectra were fitted using the equivalent circuits of figure 65. This electrical circuit was adopted to identify the different contribution to the resistance of the cell. The equivalent circuit presents an inductive element L_1, which is due to the set-up. Furthermore, a serial resistance R_s was inserted to consider all the ohmic contributions (e.g., ionic conductivity of the electrolyte). Finally, three ZARC elements (a resistance R_i in parallel with a Constant Phase Elements Q_i) where considered for the polarization contributions. The equivalent circuit was chosen as the simplest circuit to fit the impedance spectra and due to the symmetrical configuration of the experiments. Therefore, the R_iQ_i elements are not necessarily be directly correlated to specific physical phenomena.

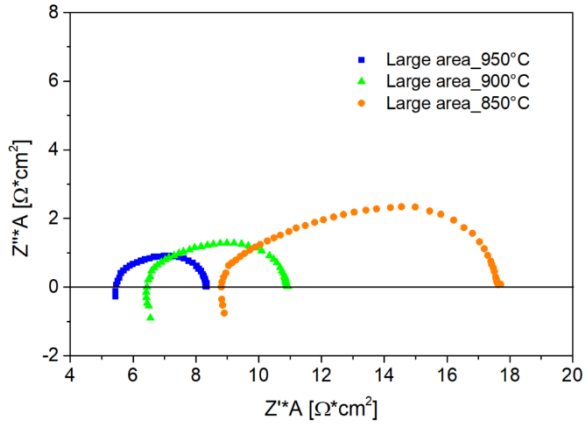

Figure 63| Impedance spectra measured for the large area cell in the high temperature range (950-850°C)

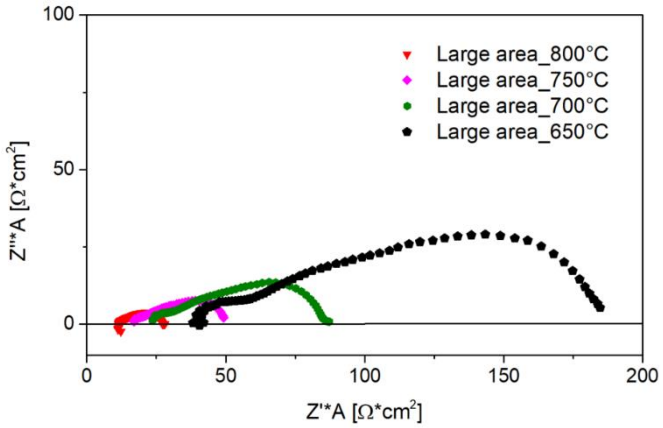

Figure 64| Impedance spectra measured for the large area cell in the low temperature range (800-650°C).

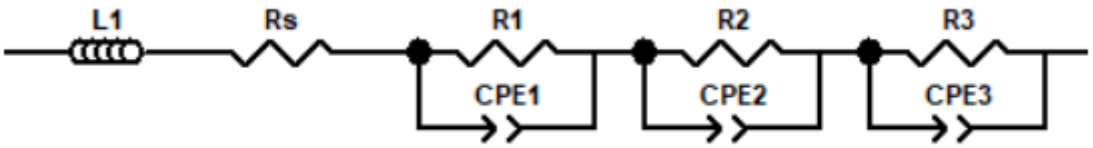

Figure 65| Equivalent circuit used for EIS fitting. The circuit is composed of one inductance L1, a serial resistance Rs and three ZARC elements ($R_i - Q_i$)

The serial and the polarization resistances (ASR) from fitted data are plotted in figure 66 and figure 67, respectively. The activation energy calculated for the Arrhenius plots is 0.72 eV ±0.01 for the serial resistance. This value is compatible with typical values from literature, where *Masciandaro et al.* [48] reported about 0.78 eV for a 3YSZ electrolyte. At 800 °C the ASR_s presents ≈11 Ω cm^2 while at the same temperature *Masciandaro et.al.* reported ≈3.8 Ω cm^2.

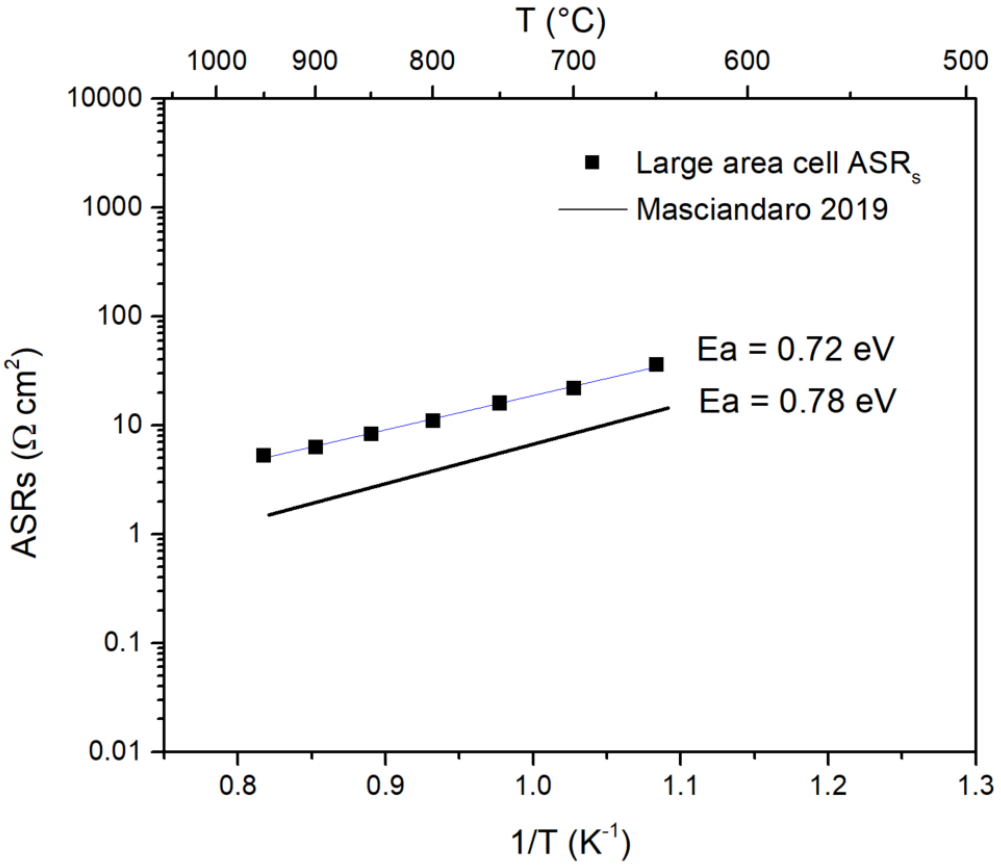

Figure 66| Arrhenius plot of the electrolyte ASR, showing the comparison between the large cell area electrolyte and Masciandro et.al..

The polarization resistance is showed in figure 66. The activation energy for the LSM/YSZ electrodes is 1.36 ±0.02 eV, whereas Murray et al. [65] highlighted about 1.17 eV for LSM/YSZ electrodes. However, other studies reported higher activation energies for electrodes of the same type as high as ≈1.5 eV [66]. At 800 °C ASR_{pol} presented ≈8 Ω cm^2 while Murray highlighted ≈0.8 Ω cm^2. This difference respect to the literature is consistent considering that the electrode

used was not optimized and it was deposited by hand brushing on top of the cell. As already mentioned, three R_iQ_i elements were used to fit the impedance spectra. The high frequency contribution R_3Q_3 ($\approx 10^4$ Hz) presented a capacitance value between 10^{-6}-10^{-7} F cm^{-2}, while the middle frequency R_2Q_2 ($\approx 10^2$ - 10^3 Hz) and the low frequency R_1Q_1 ($\approx 10^1$ – 10^2 Hz) contributions presented a capacitance value between 10^{-5} F cm^{-2} and 10^{-3}-10^{-4} F cm^{-2}, respectively. The low frequency capacitance value could be attributed to the reactions at the surface of LSM, which is typical a limiting step for these electrodes [67]. Regarding the middle and high frequency range, the accumulation phenomenon could be attributed to mass transport [68].

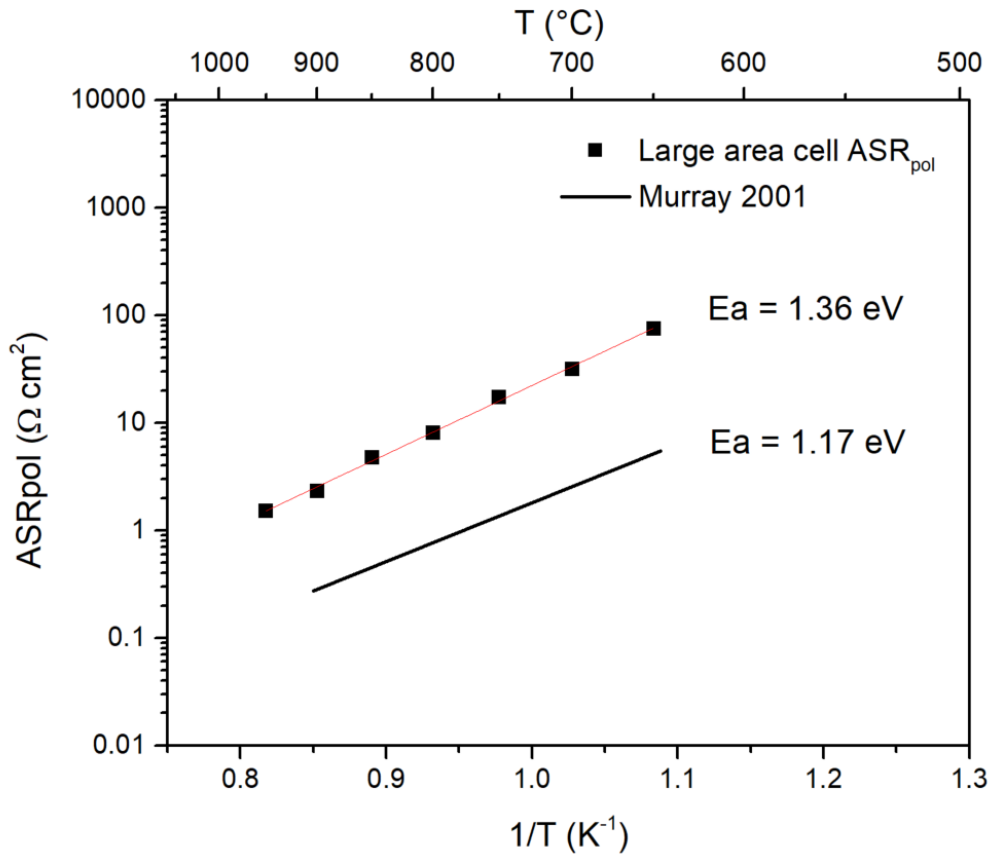

Figure 67| Arrhenius plot of the polarisation ASR. In the figure is shown the comparison with the large cell area polarisation resistance and the reference Murray 2001.

In order to understand the lower performance of the cell compared to the references, a SEM analysis was carried out to observe the electrolyte microstructure. As shown in figure 68, the 3YSZ electrolyte presented some pores, smaller than 1 μm but which affected the ionic conductivity and gas tightness, typically requirements of this component. To this end, the difference in terms of ASR_s compared to literature was attributed to the sintering thermal treatment. The sintering temperature of 1450°C will have to be further optimised to achieve the expected density of the electrolyte.

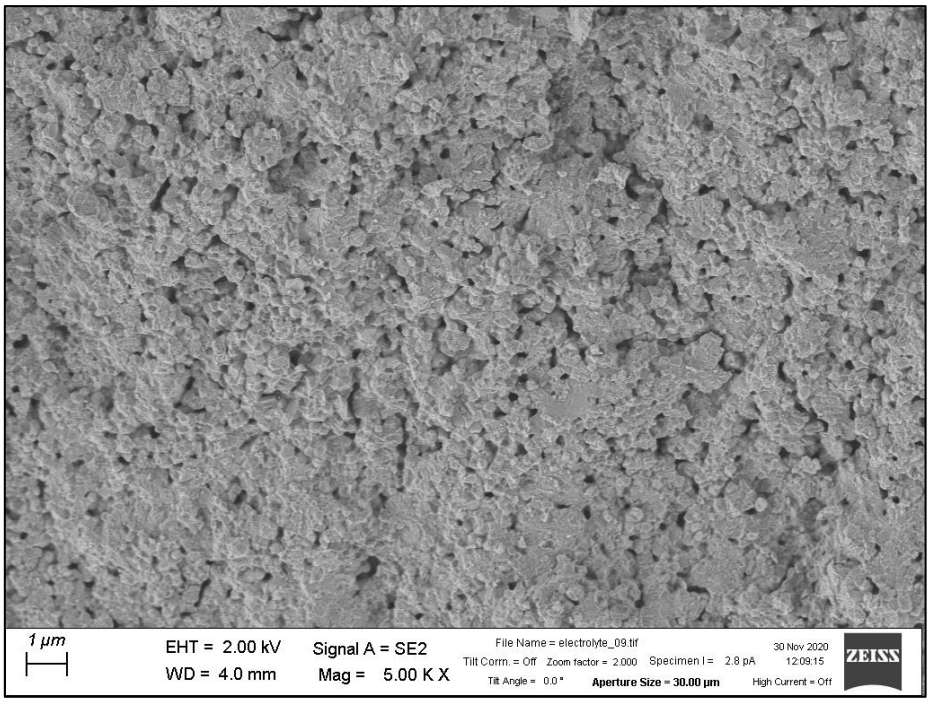

Figure 68| SEM image of the 3YSZ electrolyte. In the picture it is possible noticed the small pores (<1µm) of the electrolyte which affects its performances.

5.2 Spiral considerations: the potential of complex shapes for functional ceramics

The spiral design has not yet been tested electrochemically as has the large area cell. However, it is already possible open discussion about the expected evolution. This innovative geometry is characterised by an external diameter about 17.8 mm. The pitch of the spiral membrane is 8 mm and the active area covered along the height of 28 mm is 1466 mm^2. Even though for demonstration purposes it was decided to start with a highly simplified design, it is noteworthy remark that this spiral has an active area close to that of a similar sized tubular cell (94%). The simplifications in this design were made purely in the direction of post-processing simplification (mainly cleaning), and it is still far from the resolution limits of this printer.

Further modifications and progress towards the more complex and tighter original design can be made when cleaning of the part is enhanced or avoided. By approaching the area of the spiral to the area of a disc, doubling the diameter increases the area quadratically, which indicates that the power increases 4 times. By taking into account the same sample height but with half spiral pitch and double diameter, the area is eight times as large. A simple tubular cell with these dimensions reaches an active area about 3000 mm^2, whereas the spiral design 11000 mm^2. This corresponds to yield surface about 375%.

Moreover, considering the latest studies on corrugated electrolyte membranes [69], which increase the active area, and so the power, about 57% compared to a simple flat electrolyte, in this case the spiral geometry could achieve an active area close to 18000 mm^2. In this regard, a yield surface of about 600% may be achieved.

By taking as a reference a standard tubular cell [70] with the same electrolyte material and using the most used electrodes as Ni-YSZ cermet anode and LSM-YSZ cathode, this can reach a power density about 522 mW/cm^2, where cathode impregnation with PdO can increase it to about 1200 mW/cm^2. Now, considering that the power of this device is proportional to the active area, only changing the geometry of this device, the spiral geometry could reach an expected value of around 7000 mW/cm^2.

Chapter 6 | Conclusions

The main goal of the current thesis was to determine and explore new concepts for Solid Oxide Cells fabrication. The thesis was focused on the Additive Manufacturing fabrication of standard dimension flat cell and functionalisation of an innovative spiral design. The cells were fabricated with the SL technology, characterised by high part accuracy and high surface finish.

Flat large area cells based on 3YSZ self-supporting electrolyte were successfully fabricated and post-processed by heat tretament. The sintered electrolytes were coated with cathode material on both sides (LSM-YSZ) and successfully characterised electrically at the operating temperatures (950-650°C). The capability of the proposed technique to produce large cells was therefore demonstrated. The electrical analysis shows lower but comparable electrochemical performances with cells already built through the SL technology. While *Masciandaro et.al* at 800 °C reported an $ASR_s \approx 3.8\ \Omega\ cm^2$, the fabricated large area electrolyte presented $\approx 11\ \Omega\ cm^2$ at the same temperature, the difference in values being negligible due to the same order of magnitude. Therefore, the lower performances were attributed to the thermal treatment that could be easily improved for example by changing the sintering temperature. After sintering optimisation, simultaneously electrolyte and electrodes fabrication in one step will be carried out through the hybrid printing SL-robocasting, followed by co-firing and characterisation of the cell, to reduce the manufacturing steps and to pursue high throughput automated production and quality control.

Furthermore, the preliminary design, completed with manifolds, for spiral electrolytes was for the first time printed and post-processed with success as well using 3YSZ. The cleaning process was successful achieved, and the thermal treatments perfectly optimised. The inks for the electrodes fabrication of such designs have been improved and adjusted for these very specific needs and are now ready for further experiments. The fabricated spirals have been injected with the anode ink, where properties such as viscosity, fluidity, thermal behaviour and microstructure resulted the most suitable among the various experimental trials. Good injection and sintering of the anode slurry were obtained and further steps for characterisation, as cathode implementation and electrochemical measures, will be carried out. Afterwards the characterisation tests, the research will move on optimising the cleaning process and remove some simplification of the design.

The geometry will be optimised in terms of performances. Smaller spiral pitch, corrugated membrane and bigger diameter can be implemented to increase the active area of the cell and the gas flows exploitation. Moreover, smaller membrane thickness will be adopted to reduce the electrolyte resistance.

This thesis has provided a deeper insight into the potential of AM technique for electrochemical device fabrication.

The present study lays the groundwork for future research into 3D printing technique as a viable and effective alternative to reduce the fabrication steps and to enhance the already noteworthy performances of SOCs. Further studies need to be carried out in order to validate the proposed design (thickness, tolerance factor etc..) especially considering the link with different sintering temperatures, when considering the whole cell processing.

Bibliography

[1] J.O.Abe et.al, "Hydrogen energy, economy and storage: Review and recommendation," *International Journal of Hydrogen Energy,* vol. 44, no. 29, pp. 15072-15086, 2019.

[2] United Nations Framework Convention on Climate Change - UNFCCC.

[3] Intergovernmental Panel on Climate Change (IPCC), 10/11/2020.

[4] Intergovernmental Panel on Climate Change (IPCC), "AR5- CLIMATE CHANGE 2013 - The Physical Science Basis," 2013.

[5] World Nuclear Association, "Heat Values of Various Fuels," 09/11/2020.

[6] International Energy Agency - IEA, "The Future of Hydrogen," 2019.

[7] IRENA, "Idrogeno da energia rinnovabile," 2019.

[8] International Energy Agency - IEA, "Technology Roadmap - Hydrogen and Fuel Cells," 2015.

[9] Energy Efficiency & Renewable Energy, "Alternative fuel data center".

[10] Iain Staffell et.al, "The role of hydrogen and fuel cells in the global energy system," *Royal Society of chemistry,* vol. 12, pp. 463-491, 2019.

[11] Emanuele Giglio et. al, "Synthetic natural gas via integrated high-temperature electrolysis and methanation: Part I—Energy performance," *Journal of Energy Storage,* vol. 1, pp. 22-37.

[12] The New York times, "California Is Trying to Jump-Start the Hydrogen Economy," 2020.

[13] Kevin Kendall et.al, High-Temperature Solid Oxide Fuel Cells for the 21st Century : Fundamentals, Design and Applications, 2015.

[14] International Renewable Energy Agency -IRENA, "Power-to-X solutions," 2020 - 11 - 29.

[15] J.M. Andu´ jar et.al, "Fuel cells: History and updating. A walk along two centuries," *Science direct,* no. 13, p. 2309–2322, 2009.

[16] B. Energy, "A Primer to Understanding Fuel Cell Power Module Life".

[17] Stephen J. McPhail et. al, "THE YELLOW PAGES OF SOFC TECHNOLOGY - International Status of SOFC deployment," IEA, 2017.

[18] M. Ronchetti, "CELLE A COMBUSTIBILE -Stato di sviluppo e prospettive della tecnologia," Enea, 2008.

[19] Muneeb Irshad et. al, "A Brief Description of High Temperature Solid Oxide Fuel Cell's Operation, Materials, Design, Fabrication Technologies and Performance," *Applied sciences,* vol. 6, no. 75, pp. 1 - 23, 2016.

[20] Tuoma Hakala et.al, "INNOSOFC STATIONARY FC: GOING LOCAL".

[21] Andrea Lanzini et.al, "DEMOnstration of large SOFC system fed with biogas from WWTP," 2017.

[22] D. P. B. A. G. Stamatis, "Improving hybrid SOFC-GT systems performance through turbomachinery design," *Energy research,* pp. 1975-1986, 2014.

[23] M.A.Laguna-Bercero, "Recent advances in high temperature electrolysis using solid oxide fuel cells: A review," *Journal of Power Sources,* vol. 203, pp. 4-16, 2012.

[24] Mahrokh Samavati et.al, "Thermodynamic and economy analysis of solid oxide electrolysersystem for syngas production," *Energy,* 2017.

[25] Vikrant Venkataraman et.al, "Reversible solid oxide systems for energy and chemical applications – Review & perspectives," *The Journal of Energy Storage,* 2019.

[26] OsakaGas, 15/12/2020.

[27] Norbert H. Menzler et.al, "Post-test characterization of a solid oxide fuel cell after more than 10 years of stack testing," *Journal of Power Sources,* pp. 1 - 10, 2020.

[28] Agarwal et.al, "An overview of degradation in solid oxide fuel cells-potential clean power sources," *Journal of Solid State Electrochemistry,* vol. 24, pp. 1239 -1270, 2020.

[29] Christian Lenser et.al, "Solid oxide fuel and electrolysis cells," *Advanced Ceramics for Energy Conversion and Storage,* pp. 1-574, 2020.

[30] NeelimaMahato et.al, "Progress in material selection for solid oxide fuel cell technology: A review," in *Progress in Materials Science*, vol. 72, 2015, pp. 141-337.

[31] Paul A. Connor et. al, "Tailoring SOFC Electrode Microstructures for Improved Performance," *Advanced Energy Materials,* vol. 8, 2018.

[32] Meilin Liua et.al, "Rational SOFC material design: new advances and tools," *Materialstoday,* vol. 14, no. 11, pp. 534-546, 2011.

[33] Jouni Puranen et.al, "Post-mortem evaluation of oxidized atmospheric plasma sprayed Mn–Co–Fe oxide spinel coatings on SOFC interconnectors," *International Journal of Hydrogen Energy,* vol. 39, pp. 17284-17294, 2014.

[34] FAE, "CELL3DITOR," 2016.

[35] T. Li et.al, "Testing of electrodes, cells and short stacks," *Elsevier,* 2016.

[36] Mark Weimar et.al, "Cost Study for Manufacturing of Solid Oxide Fuel Cell Power Systems," 2013.

[37] L. Bernadet et.al, "Reversible fuel electrode supported Solid Oxide Cells fabricated by aqueous multi-layered tape casting".

[38] J. Izdebska and S. Thomas, Printing on Polymers - Fundamentals and Applications, 2016.

[39] F. Rita, "Printing processes dedicated for the mass production of ceramic based microelectronic devices," 2012.

[40] D. Medvedev et.al, "A tape calendering method as an effective way for the preparation of proton ceramic fuel cells with enhanced performance," *Electrochimica Acta,* vol. 210, pp. 681-688, 2016.

[41] R.E.Sousa et.al, "High performance screen printable lithium-ion battery cathode ink based on C-LiFePO4," *Electrochimica Acta,* vol. 196, pp. 92-100, 2016.

[42] Stephen J. McPhail et.al, "A new all-European technology for clean, efficient power," 2017.

[43] qsofc.eu, "Automated mass-manufacturing and quality assurance of Solid Oxide Fuel Cell stacks," 2017.

[44] H. 2020, "Next Generation solid oxide fuel cell and electrolysis technology".

[45] S. Mohammad e.al., "The potentials of additive manufacturing for mass production of electrochemical energy systems," *Current Opinion in Electrochemistry,* no. 20, pp. 54-59, 2020.

[46] Tuan D. Ngo et.al., "Additive manufacturing (3D printing): A review of materials, methods,applications and challenges," *Composites Part B,* vol. 143, pp. 172-196, 2018.

[47] Charles W. Hull, "Apparatus for production of three-dimensional objects by stereolithography," 1986.

[48] S. Masciandaro et.al, "Three-dimensional printed yttria-stabilized zirconia self-supported electrolytes for solid oxide fuel cell applications," *Journal of the European Ceramic Society,* 2017.

[49] Lim Chin Hwa et.al., "Recent advances in 3D printing of porous ceramics: A review," *Current Opinion in Solid State and Materials Science,* vol. 21, pp. 323-347, 2017.

[50] J. C. Ruiz-Morales et.al, "Three dimensional printing of components and functional devices for energy and environmental applications," *Energy Environ. Sci.,,* no. 10, pp. 846-859, 2017.

[51] Zhangwei Chen et.al, "3D printing of ceramics: A review," *Journal of the European Ceramic Society,* no. 39, p. 661–687, 2018.

[52] Z. J. e. Pan Jiang, "Recent advances in direct ink writing of electronic components and functional devices," *Springer Nature,* 2017.

[53] Yubai Zhang et.al, "Recent Progress of Direct Ink Writing of Electronic Components for Advanced Wearable Devices," *ACS Applied Electronic Materials,* no. 9, pp. 1718-1734, 2019.

[54] Erwin Peng et.al, "Robocasting of dense yttria-stabilized zirconia," *J Mater Sci,* no. 53, pp. 247 - 273, 2018.

[55] Nahum Travitzky et.al, "Additive Manufacturing of Ceramic-Based Materials," *Advanced Engineering Materials,* vol. 16, no. 6, pp. 729-754, 2014.

[56] Diego Manfredi et.al, "From Powders to Dense Metal Parts: Characterization of a Commercial AlSiMg Alloy Processed through Direct Metal Laser Sintering," *Materials,* pp. 856-869, 2013.

[57] Erwin Peng et.al, "Ceramic Robocasting: Recent Achievements, Potential, and Future Developments," *Advanced Materials,* 2018.

[58] Leng et.al, "Direct Ink Writing Based 4D Printing of Materials and Their Applications," *Advanced Science,* no. 7, pp. 1 - 29, 2020.

[59] Custompart.net, 30/10/2020.

[60] Cesar Parra Cabrera et.al, "3D printing in chemical engineering and catalytic technology: structured catalysts, mixers and reactors," *Chem Soc Rev,* no. 47, pp. 209 - 230, 2018.

[61] Institut de Recerca en Energia de Catalunya IREC.

[62] Gibson, "Photopolymerization processes, from Additive Manufacturing technologies," 2010.

[63] Digitalfire.com, "A Low Cost Tester of Glaze Melt Fluidity," 15/01/2021.

[64] M. et.al, "Characterisation of fuel cell state using Electrochemical Impedance Spectroscopy analysis".

[65] E. Perry Murray et.al, "(LaSe)MnO3-(Ce,Gd)O2 composite cathodes for solid oxide fuel cells," *Solid state ionics,* vol. 143, pp. 265-273, 2001.

[66] Erica PerryMurray et.al., "Oxygen transfer processes in (La,Sr)MnO3/Y2O3-stabilized ZrO2 cathodes: an impedance spectroscopy study," vol. 110, no. 4, pp. 235-243, 1998.

[67] Jae-Dong Kim et.al., "Characterization of LSM–YSZ composite electrode by ac impedance spectroscopy," vol. 143, pp. 379-389, 2001.

[68] Eunseo Lee et.al., "Determination of the rate-determining step of the oxygen reduction reaction of La0.8Sr0.2MnO3(LSM)- 8mol% yttria-stabilized zirconia(YSZ): Composition and microstructure," no. 2, pp. 1792-1797, 2021.

[69] Arianna Pesce et.al, “3D printing the next generation of enhanced solid oxide fuel and electrolysis cells,” *Journal of Materials Chemistry A,* vol. 8, 2020.

[70] Nan-Qi Duan et.al, “High performance anode-supported tubular solid oxide fuel cells fabricated by a novel slurry-casting,” *Scientific reports,* vol. 5, 2015.